

## Radial Gradients and Intrinsic Scatter in MaNGA Galaxies

TATHAGATA PAL<sup>1</sup> AND GUY WORTHEY<sup>1</sup>

<sup>1</sup> *Washington State University  
Department of Physics and Astronomy, Webster Hall  
100 Dairy Road Room 1245, Pullman  
WA 99164*

Submitted to ApJS

### ABSTRACT

We derive stellar population parameters and their radial gradients within  $0.65 R_e$  for spatially resolved spectra of 2417 early-type galaxies from the MaNGA survey with stellar velocity dispersions ( $\sigma$ ) between  $50 \text{ km s}^{-1}$  and  $340 \text{ km s}^{-1}$ . We invert a grid of metallicity-composite stellar population models to find mean age and the abundances of C, N, Na, Mg, and Fe. These models have significant improvements compared to past models, including isochrones that respond to individual element abundances.

Globally, age rises with  $\sigma$  while  $[\text{Fe}/\text{H}]$  gently falls. Individual light element abundances strengthen with  $\sigma$  but strengthen faster for  $\log(\sigma) > 2.0$ .  $[\text{Fe}/\text{H}]$  shows a maximum at  $\log(\sigma) \approx 2.0$ , falling to either side. Light element  $[\text{X}/\text{Fe}]$  anticorrelate with  $[\text{Fe}/\text{H}]$ . Heterogeneity as measured by astrophysical scatter is highest in low- $\sigma$  galaxies, most dramatically for age, Fe, and N.

For galaxy-internal parameters, age shows nearly flat radial gradients in low- $\sigma$  galaxies, slightly negative at high  $\sigma$ . The mean radial gradient in  $[\text{Fe}/\text{H}]$  is negative and light element  $[\text{X}/\text{Fe}]$ s fall. Intrinsic scatter in gradients is highest in high- $\sigma$  galaxies, most dramatically for age and Fe. Evidently, nearly as many galaxies form inside-out as form outside-in.

A near-zero radial gradient in age and light elements coupled with a mild  $[\text{Fe}/\text{H}]$  gradient supports the hierarchical merging scenario for ETG evolution. IllustrisTNG hierarchical simulations reproduce the age structure we find, show the abundance slope changes at  $\log(\sigma) \approx 2.0$  that we observe, and exhibit flat gradients similar to those we derive, although the abundances predicted by IllustrisTNG are significantly higher than our observations overall.

**Keywords:** Galaxy abundances (574) — Galaxy ages (576) — Galaxy chemical evolution (580) — Galaxy evolution (594) — Galaxy stellar content (621)

### 1. INTRODUCTION

The evolution of the chemical properties of stellar populations, as well as the interstellar and intergalactic medium across cosmic epochs, offers valuable insights into the processes that drive galaxy formation and evolution. A wide range of models and cosmological simulations have been created to explore the evolution of the baryonic matter, star formation processes, and the characteristics of galaxies throughout cosmic history, including in the local

universe (Springel et al. 2005; Vogelsberger et al. 2014a; Somerville & Davé 2015; Schaye et al. 2015; Nelson et al. 2019). The abundances of certain heavy elements relative to hydrogen put strong constraints on these models. The metal content of galaxies, often tracked via  $[\text{Fe}/\text{H}]$ , reflects heavy elements added by supernovae and other stellar sources such as nucleosynthetically-enriched mass loss and neutron star mergers minus the amount of metals removed through mechanisms such as outflows and stripping (Tremonti et al. 2004; Finlator & Davé 2008; Peeples & Shankar 2011; De Rossi et al. 2015; Chisholm et al. 2017). Heavy element abundances are also affected by dilution caused by inflows of pristine gas. Iron is a key element in understanding the evolution of galaxies (Kereš et al. 2005;

Davé et al. 2011; Sánchez Almeida et al. 2014) but various other chemical elements are formed over different timescales by different types of stars. The hope is that their relative abundances can be translated into the star formation history and chemical evolution within a galaxy (Tinsley 1979; Matteucci 1996; Thomas et al. 2003; Nomoto et al. 2013; Weinberg et al. 2017).

Analyzing [Fe/H] and chemical abundances on spatially resolved scales, often summarized as radial gradients, may provide further insight into the processes that have shaped the growth and assembly of galaxies (Zaritsky et al. 1994; Rawle et al. 2010; Li et al. 2013; Goddard et al. 2017; La Barbera et al. 2017; Esteban et al. 2020). Studies on [Fe/H] and elemental abundance gradients also offer information on whether galaxies formed “inside-out” or “outside-in” (Chiappini et al. 1997; Garnett 2004; Kobayashi & Nakasato 2011), and elucidate the role of internal processes such as galactic fountains, stellar migration, and radial gas inflows (Dekel & Silk 1986; Sellwood & Binney 2002; Oppenheimer & Davé 2008; Roškar et al. 2008b,a; Spitoni et al. 2009; Meilioli et al. 2015).

The formation history and evolution of galaxies remain a subject of considerable debate. Two prominent scenarios provide convenient bookends for discussion. The *monolithic collapse* hypothesis suggests that galaxies form from the dissipation of large, pre-galactic gas clouds, leading to the formation of all their stars in one fairly brief event (Larson 1974, 1976; Thomas et al. 1999; Pipino et al. 2010). According to this model, galaxies are predicted to form via “outside-in” formation, where star formation in the outermost regions ceases earlier due to the earlier onset of galactic winds in areas with shallower gravitational potential wells (Pipino et al. 2006). Conversely, the *hierarchical merger* hypothesis proposes that large galaxies form through the merging of smaller subunits (Kauffmann et al. 1993; Kauffmann & Charlot 1998; De Lucia & Blaizot 2007). In this scenario, star formation is an ongoing process that depends on the gas content of the progenitor galaxies. Galaxies formed through the merging of smaller units tend to have flattened [Fe/H] gradients (White 1980; Di Matteo et al. 2009). In contrast, galaxies formed through dissipative processes are expected to have steep to moderate gradients in [Fe/H] and other heavy element abundances (Larson 1976; Carlberg & Freedman 1985). There have also been studies where the fundamentals of both of these theories are shown to be partially true (Mehlert et al. 2003; Ogando et al. 2005; Goddard et al. 2017). An overview of both of these theories can be found in Sil’chenko (2015).

The most efficient way to extract information from galaxy spectra is through stellar population analysis, which provides details on age, [Fe/H], and individual element abundances for the galaxy in question. For such analysis,

we can employ either the full spectrum fitting technique (Koleva et al. 2009a; Conroy et al. 2014, 2018) or absorption index measurements (Trager et al. 1998; Serven et al. 2011; Johansson et al. 2012). There is no fundamental difference between the two approaches. It is merely a question of at which stage empirical adjustments are imposed. Because synthetic stellar spectra match empirical spectra poorly (Martins & Coelho 2007), but because control over individual elements has become essential, some form of forced matching between synthetic and observed stellar spectra is required. The use of indices, adopted for this work, allow an average over many stellar spectral libraries at a variety of instrumental resolutions prior to the empirical zeropointing, at cost of operating within a predefined set of diagnostic indices.

Stellar population analysis works at all redshifts. It is an important tool in analyzing the chemical compositions of the galaxies that hold clues to the galaxy formation and evolution over many epochs of time (Walcher et al. 2011; Conroy 2013). It is possible that formation time-scales in galaxies can be measured via the ratio of  $\alpha$ -elements to that of heavy metals (Fe-peak elements) (Thomas et al. 1999), although the high-mass initial mass function (IMF) may potentially also alter it (Worthey et al. 1992, 2014). Abundances of other lighter metals like carbon (C) and nitrogen (N) put constraints on star formation timescale and also gas inflow (Chiappini et al. 2003; Johansson et al. 2012; Berg et al. 2019). Spectral analysis of galaxies have also been shown to be effective in constraining the slope in the low-mass IMF of galaxies (Martín-Navarro et al. 2015; van Dokkum et al. 2017; Parikh et al. 2018).

The majority of existing studies has concentrated on detailed stellar population analysis of Early-Type Galaxies (ETGs). This focus is due to the fact that ETGs can be more accurately modeled using simple star formation histories, as they typically exhibit no ongoing star formation (Bruzual & Charlot 2003; Vazdekis et al. 2010; Worthey et al. 2014) and thus allow analysis of Balmer features that are otherwise susceptible to emission line fill-in. ETGs are predominantly composed of older stars, with minimal or no current star formation activity. In favorable cases, at least, they have had only modest changes over much of cosmic time, and present themselves as good laboratories for studying the long-term evolution of stellar populations.

The study of gradients in various parameters has long been used as a mean to understand the formation and evolution of galaxies. Two of the first studies available in literature on color gradients were done by Tinsley & Larson (1977) and Franx & Illingworth (1990). In the early 1990s, a number of pioneering studies were published on line strength gradients, by Peletier (1989); Gorgas et al. (1990), Bender & Surma (1992), Davies et al. (1993), and

others. The first mention of an  $[\text{Fe}/\text{H}]$  gradient (as opposed to a line strength gradient unattached to the solar-zeroed  $[\text{Fe}/\text{H}]$  standard) that we found in literature is by [Carollo et al. \(1993\)](#) where they measured line strengths of different features from 42 ETGs to infer an  $[\text{Fe}/\text{H}]$  gradient. These studies did not necessarily use any stellar population model to infer age,  $[\text{Fe}/\text{H}]$ , or element abundances but they pioneered the field of gradient studies. Later on with the development reliable stellar population models, a large number of studies had been completed on spatial gradients in age,  $[\text{Fe}/\text{H}]$ , and element abundances within both ETGs and Late Type Galaxies (LTGs) ([Mehlert et al. 2003](#); [Forbes et al. 2005](#); [Proctor et al. 2005](#); [Jablonka et al. 2007](#); [Spolaor et al. 2009](#); [Rawle et al. 2010](#); [Kuntschner et al. 2010](#); [González Delgado et al. 2017](#); [Goddard et al. 2017](#); [Parikh et al. 2018](#); [Feldmeier-Krause et al. 2021](#); [Parikh et al. 2021](#)). These studies generally agree that ETGs and the bulges of spiral galaxies display negative  $[\text{Fe}/\text{H}]$  gradients, while showing small positive or flat gradients in both age and the  $\alpha/\text{Fe}$  ratio. This “globalness” of age and  $\alpha$  throughout the body of the galaxy is an example of a useful constraint to be matched by galaxy formation models.

With the emergence of Integral Field Unit (IFU) surveys for galaxies opens up the scope of using high quality data to investigate gradients in stellar population parameters further. Such surveys include the SAURON and ATLAS-3D project ([Bacon et al. 2001](#); [Emsellem et al. 2004](#); [Cappellari et al. 2011](#)), CALIFA project ([Sánchez et al. 2012](#)), SAMI project ([Croom et al. 2012](#)), and MaNGA project ([Bundy et al. 2015](#)). IFU spectroscopy allows us to get galaxy spectra from different parts of the galaxy enabling detailed radial studies. Although these surveys provide us with a large volume of data, most of the studies till date are either limited by sample size (highest number of individual galaxies studied till date is by [Goddard et al. \(2017\)](#) where they studied around 700 ETGs and [Ferreras et al. \(2019\)](#) analyzing around 500 ETGs) or use the spectra stacking technique ([Parikh et al. 2018](#)) which when used loses the individual information of a galaxy. Some other studies also treat each galaxy individually but they are severely restricted in terms of sample size ([Greene et al. 2015](#); [Alton et al. 2018](#); [Feldmeier-Krause et al. 2021](#)). In this work, we consider 2417 individual unique galaxies from the Mapping Nearby Galaxies at Apache Point Observatory (MaNGA, [Bundy et al. \(2015\)](#)) for detailed study on the age,  $[\text{Fe}/\text{H}]$ , and element abundances along with their corresponding gradients.

The stellar population models employed are based on the framework established by [Worthey \(1994\)](#), incorporating the index definitions expanded by [Sereno et al. \(2005\)](#), and further refined following [Worthey et al. \(2011\)](#). One of our focuses is on the age,  $[\text{Fe}/\text{H}]$ , and C, N, sodium

(Na), and magnesium (Mg) abundances for the galaxies and their dependence on stellar velocity dispersion ( $\sigma$ ) and  $[\text{Fe}/\text{H}]$  (for abundances only). We take a deep dive into the radial gradients in those parameters and how they are changing with  $\sigma$ . Alongside these, we also calculate the intrinsic scatter ( $\delta_i$ ) in all the measured quantities and discuss the results.

It is important to state at the outset a couple of important recent improvements in the models that separate these results from previous work. First, the isochrones upon which the models rest now vary with individual element abundances ([Worthey et al. 2022](#)). This enables an effect we term “magnesium amplification” that applies to Mg and other elements as well. Addition of Mg, alone, to the chemical mixture in a stellar population, will add opacity to the stars, increase their radii, and cool them. Cooler stars have stronger Mg lines. So, not only will Mg line strengths increase due to the increased number of absorbers, Mg lines will also increase in strength due to arising in cooler stars. Since inclusion of this effect is new to the field starting with this work, our results will not necessarily agree with previous estimates of quantities such as  $[\text{Fe}/\text{H}]$ ,  $[\text{C}/\text{Fe}]$ , or  $[\text{Mg}/\text{Fe}]$ . Second, we incorporate an abundance distribution function (ADF) instead of a delta function in abundance ([Tang et al. 2014](#)). It is important to do this because metal-poor populations are brighter in the blue, and thus dilute metallic lines found in that spectral region. In the red, the balancing favors metal-rich populations more. We parameterize by the peak (mode) of the ADF, not by, for example, the  $V$ -weighted average abundance, or, for example, the mass-weighted average abundance. This introduces modest, well-behaved offsets between results derived from a simple stellar population (SSP) and this work, as illustrated in [Tang et al.](#)

The influence of uncertainties in stellar population modelling has been well documented by [Conroy et al. \(2009\)](#). A lot of fundamental work was also done in 1990s on the effect of intrinsic scatter in ETGs ([Gregg 1992](#); [Guzman et al. 1993](#)). A lot of references regarding the effect of the intrinsic scatter on the Fundamental Plane (FP) relationship can be found in literature ([Forbes et al. 1998](#); [Blakeslee et al. 2009](#); [Hyde & Bernardi 2009](#); [Magoulas et al. 2012](#); [D’Eugenio et al. 2024](#)). By including  $[\alpha/\text{Fe}]$  as a fourth parameter in the FP, [Gargiulo et al. \(2009\)](#) showed that the total scatter reduces from 0.088 to 0.075 dex, while the estimated intrinsic scatter decreases from 0.068 to 0.049 dex. [Falcón-Barroso et al. \(2011\)](#) quantified intrinsic scatter in scaling relations for nearby elliptical galaxies.

However, the intrinsic, astrophysical scatter in age,  $[\text{Fe}/\text{H}]$ , and elemental abundances are not well documented in previous literature. We wanted to better this sit-

uation and thus treated each MaNGA galaxy in our study individually (not using any kind of stacking algorithm).

This article is arranged as follows: §2 explains the source and type of data used in this work, §3 contains the details of the analysis performed along with brief explanation of the stellar population model used for this work, §4 elucidates all of our results, §5 discusses the implications of our results and comparison with previous works, and also discusses our results on the intrinsic scatter. §6 concludes the article with reiterating our main results and forecasting future work, and an appendix gives a library of graphical comparisons with the TNG-100 cosmological evolution simulation, part of tables elucidating all the indices used in this work and result of the inversion program COMPFIT.

## 2. DATA

In this section we explain the source and features of the data used in this work. Broadly, we use stellar population analysis with the MaNGA DR17 IFU data to extract information on age, [Fe/H], and abundance of different elements and also their corresponding gradients.

### 2.1. MaNGA Data

MaNGA, part of the Fourth-Generation Sloan Digital Sky Survey (SDSS IV, [Blanton et al. \(2017\)](#)), aims to comprehensively chart the chemical composition and kinematics of nearby galaxies. Using integral field unit (IFU) spectroscopy, MaNGA captures spectra across a large number of locations within each galaxy ([Bundy et al. 2015](#)). The observations from the IFUs ([Drory et al. 2015](#)) are fed into the BOSS spectrographs ([Smee et al. 2013](#)) mounted on the Sloan telescope ([Gunn et al. 2006](#)) at the Apogee Point Observatory. For this work, we used the latest and the final data release (DR) of the MaNGA which is DR 17 ([Abdurro'uf et al. 2022](#)). The DR 17 contains IFU observations for nearly 10000 unique galaxies at a resolution of  $R \sim 2000$  covering a wavelength range from  $3000\text{\AA}$  to  $10000\text{\AA}$ .

The MaNGA Data Analysis Pipeline (DAP) provides spatially stacked spectra in form of a datacube ([Westfall et al. 2019; Law et al. 2021](#)). It also provides stellar kinematics ( $V$  and  $\sigma$ ), nebular emission line properties, and spectral indices ([Belfiore et al. 2019](#)). For this work, we subtracted the nebular emission lines that the DAP provided from all the corresponding spectrum before doing any further analysis.

Since we are interested in ETGs only, we first pick the galaxies which have elliptical morphology. It is well known for a fact that the elliptical galaxies have high Sérsic index value ( $n$ , [Sérsic \(1963\)](#)). Thus from the list of 10000 unique galaxies in MaNGA DR 17, we chose galaxies that have a value of  $n > 2$ . This left us with 6273 galaxies out of 10010 unique galaxies that the MaNGA DR 17 provides. The number distribution of all these 6273 galaxies is shown in Fig. 1.

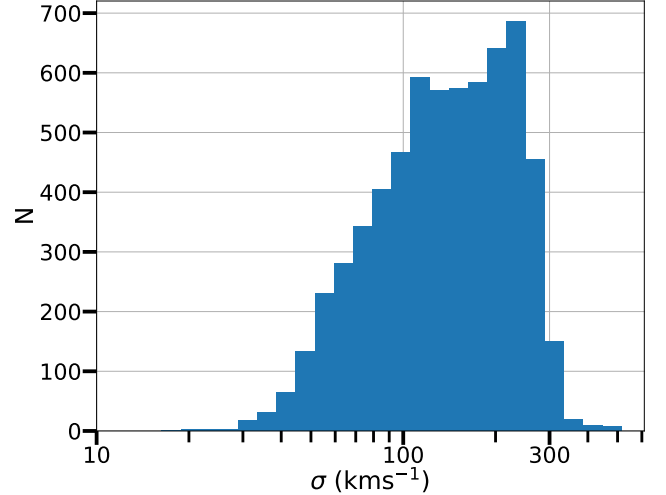


**Figure 1.** The distribution of all galaxies with  $n > 2$  as a function of velocity dispersion ( $\sigma$ ).

### 2.2. Further Filtering

After choosing 6273 galaxies from MaNGA DR 17, we discarded galaxies that had  $H_\alpha$  emission lines as we are interested only in ETGs that have very little to none star-forming activity. From the DAP datacube, if the sum of emission line flux within the  $H_\alpha$  index band is less than 15% of the sum of observed flux within the same wavelength interval, then we select that galaxy for further analysis. This left us with 5164 galaxies. The  $H_\alpha$  index band is defined to be  $6548\text{\AA} < \lambda < 6578\text{\AA}$  ([Cohen et al. 1998](#)). It is to be noted that the wavelength defined here is the restframe wavelength. In order to convert from observed to restframe wavelength we use:

$$\lambda_{rest} = \frac{\lambda_{observed}}{(1+z)(1+\frac{v}{c})} \quad (1)$$

In Eqn. 1,  $z$  is the redshift of the galaxy,  $v$  is the internal stellar velocity at the sampled location within the galaxy, and  $c$  is the speed of light. We associate a global  $\sigma$  to measure the stellar velocity dispersion at  $0.5 R_e$ . To estimate  $\sigma$  at other annuli, we use median radial gradient results from [Gonzalez \(1993\)](#). We tested our analysis by cutting this mean in half and then re-deriving population parameters and found no significant change in our outcomes. However, when applying the results for  $\sigma$  gradient in individual galaxies provided by [Illingworth \(1981\)](#), we observed substantially different results for our analysis. Given that [Gonzalez \(1993\)](#) offers  $\sigma$  gradients for a larger sample of ETGs compared to the limited data in [Illingworth \(1981\)](#), we ultimately decided to adopt the results from [Gonzalez \(1993\)](#) for our analysis. We also could have adopted an annulus mean directly from the MaNGA DAP, but intuition drove



us to use the independent mean trend to sidestep any line strength- $\sigma$  degeneracy that may exist.

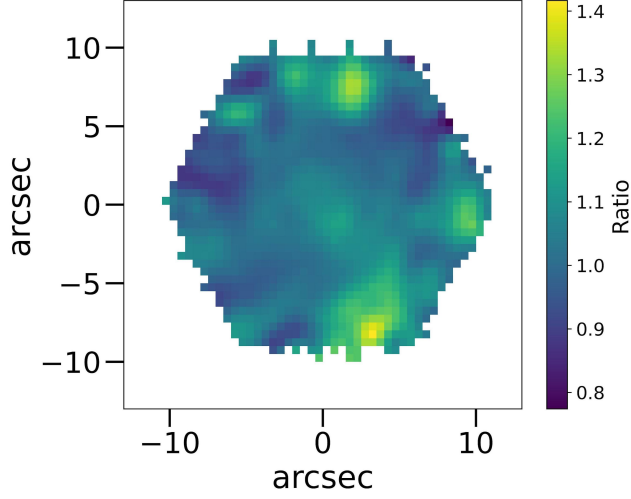


**Figure 2.** Position of the MaNGA IFU with respect to the center of the MaNGA galaxy 1-245451. The colorbar shows the ratio of mean flux within  $H_\alpha$  index band and mean flux in the continuum.

Fig. 2 shows the ratio of mean fluxes within the  $H_\alpha$  index band and the continuum for the MaNGA galaxy 1-245451. The red and blue continuum are defined to be  $6600\text{\AA} < \lambda < 6640\text{\AA}$  and  $6420\text{\AA} < \lambda < 6455\text{\AA}$  respectively (Cohen et al. 1998). The average of flux within these two continuum is taken to be the mean flux within the continuum band. Since the ratio is close to one at the location of the galaxy (see Fig. 3), it shows that the algorithm that we opted to reject galaxies with  $H_\alpha$  emission, is working optimally. All the wavelengths are converted to restframe wavelength using Eqn.1.

### 2.3. Creating Annuli

The MaNGA IFU provides us with spectroscopic data from different regions of the galaxy and the MaNGA DAP then processes this spatial and spectroscopic information into a 3D datacube. Two axes of this datacube hold positional information while the third axis gives spectroscopic information.

We divide each galaxy into 10 annuli starting from  $0.1R_e$  to  $1.0R_e$  with an increment of  $0.1R_e$ , where  $R_e$  is the effective radius of the galaxy, synonymous to the half-light radius of the galaxy for Sérsic functions. The following equation is used to define the ellipse in the galaxy's positional space.

$$\frac{[(x-h)\cos\theta + (y-k)\sin\theta]^2}{a^2} + \frac{[(x-h)\sin\theta - (y-k)\cos\theta]^2}{b^2} = 1 \quad (2)$$

In Eqn. 2,  $x$  &  $y$  are the RA and Dec respectively of the spaxel (spatial pixel) in consideration,  $h$  &  $k$  are the RA and Dec respectively of the center of the galaxy,  $\theta$  is the angle of inclination (East of North),  $2a$  &  $2b$  are the semi-major and semi-minor axes respectively of the galaxy. In this equation,  $a$  is used synonymously with  $R_e$ . The  $b$  is obtained from the  $b/a$  ratio for the galaxy in question. All of  $\theta$ ,  $a$ , and  $b/a$  come from the Sérsic profile as provided by the MaNGA DAP. It is to be noted that this system of dividing the galaxy in several annuli is motivated from the the work of Parikh et al. (2018).

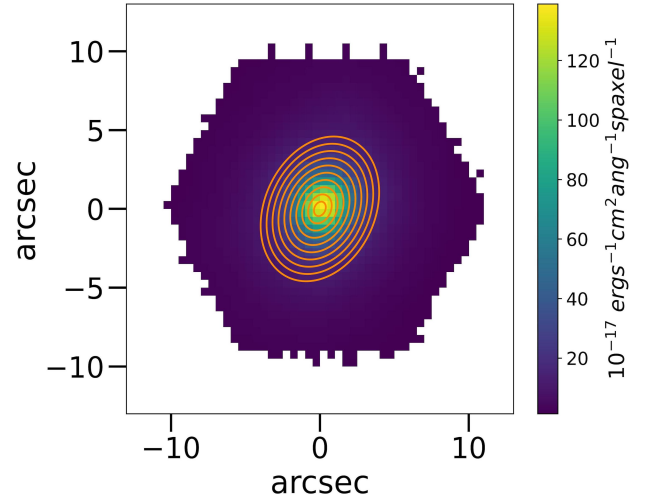


**Figure 3.** The map of  $H_\alpha$  flux within the  $H_\alpha$  index band (in absolute scale) for the MaNGA galaxy 1-245451. The orange ellipses are calculated using Eqn.2 with parameters specific to this galaxy.

Fig. 3 shows our annulus scheme. The representative spectrum for each annulus is the average spectrum for all spaxels within the same annulus. It is worth mentioning that MaNGA DAP provides masks for bad spaxels and we considered those masks while calculating the average for each annulus. The final representative spectrum is obtained the subtracting the average of the emission line spectrum from the average of the flux spectrum for each annulus. Fig. 4 shows two examples of spectra from two different regions of the galaxy. It is to be noted that we do not follow any stacking scheme. We wanted to investigate the scatter in different quantities and thus treat each galaxy individually. This possesses a problem of having very low signal-to-noise ratio in the spectrum from the peripheral region of the galaxy and also beyond  $9500\text{\AA}$  in the spectrum from any region of the galaxy. In order to mitigate this

problem, we consider only up to the 7<sup>th</sup> annulus for every galaxy for any further analysis (if you consider the center part of the galaxy as 0<sup>th</sup> annulus, then up to the 6<sup>th</sup> annulus). Also in terms of element abundance analysis, we restrict ourselves to elements that do not have indices beyond 9500Å (C, N, Na, and Mg), and also any IMF analysis based on the Wing-Ford band  $\lambda\lambda 9900$ .

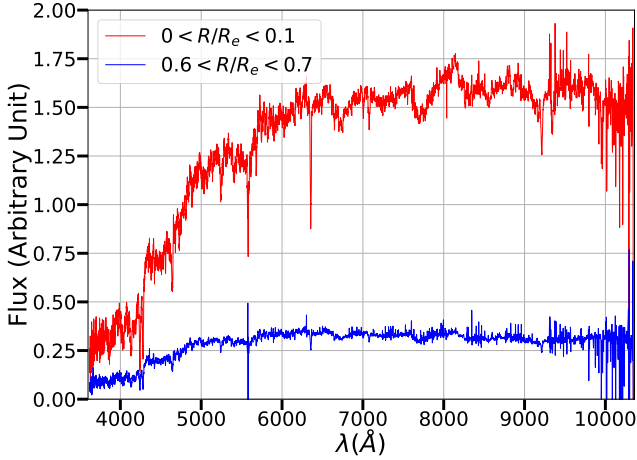


**Figure 4.** Spectra of MaNGA galaxy 1-245451 for innermost annulus (red) and 7<sup>th</sup> annulus (blue) from the center.

### 3. ANALYSIS

In this section, we explain the pipeline for analysis used in this work. All the analyses are done on each individual spectrum from a particular annulus for a given galaxy. Unlike Parikh et al. (2018), we do not stack spectra in this work. One of the main goals for this work is to look into the intrinsic scatter in different derived quantities like the age, [Fe/H], and chemical abundances (this is discussed in details in §5.3). For this reason, we treat each galaxy individually. The problem of having lower S/N ratio is mitigated using the two strategies outlined in Section 2.3.

#### 3.1. Spectral Analysis

Stellar population parameters are determined by fitting stellar population models to spectra. This can be achieved either by fitting the entire spectrum (Koleva et al. 2009b; Cappellari 2017; Conroy et al. 2018). It can also be done by focusing on specific absorption line features (Trager et al. 2000a; Schiavon 2007; Thomas et al. 2010). In this work, we adopt the latter method and concentrate on the strongest absorption features.

In §2.1 we mention the specific data products used in this work from the MaNGA DAP (Westfall et al. 2019). Currently, MaNGA DAP provides us with three different binning schemes: SPX that fits each individual spaxel with  $g$ -band S/N of at least 1, VOR10 is the Voronoi binning

with  $g$ -band S/N of at least 10 (Cappellari & Copin 2003), and HYB10 which is a mix of both SPX and VOR10 binning schemes. We use SPX type and do not use any binning scheme. In order to find out the stellar kinematics, the data was fitted with templates from the MILES HC stellar library. The MILES HC consists of 42 stellar spectra by hierarchically-clustering the spectra in the MILES stellar library (Sánchez-Blázquez et al. 2006). We use the  $\sigma$  provided by this model fit to the stellar continuum as a proxy for  $\sigma$  at 0.5  $R_e$ . The emission line fitting module uses the MASTAR stellar library (Abdurro’uf et al. 2022; Yan et al. 2019). We subtracted the emission lines from the observed spectra within each IFU before going forward with further analysis.

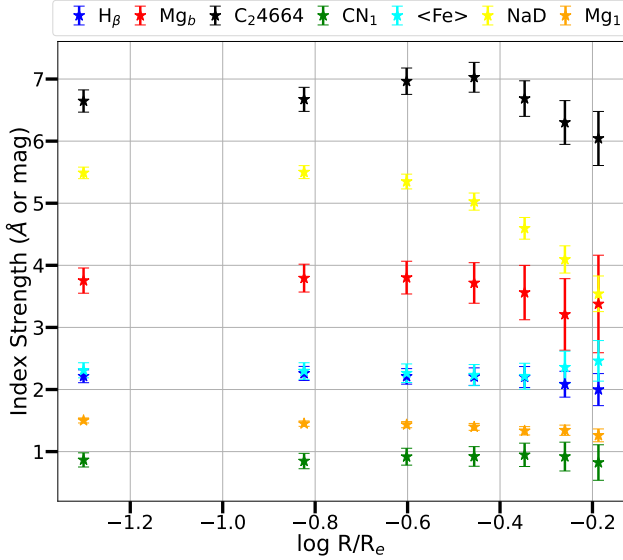
In this work, we specifically analyzed the age, [Fe/H], and chemical abundances of C, N, Na, and Mg. Several absorption spectral features are used to determine the variables in question using the model described in Section 3.2. The strengths of the absorption features used are calculated using the Equations 2 and 3 in Worthey et al. (1994). The indices used to calculate different quantities and the corresponding passbands are given in Table 1. It is to be noted that 80 features were fed into the model while calculating our desired quantities. A full list of the 80 indices is given in Appendix B. Table 1 shows the indices that strongly affects the underlying variable. For example, CN<sub>1</sub> feature mostly affects [N/R], but it also has mild effect on [C/R] as well. The “R” in this notation may stand for any generic heavy element, but for this work “R” can be interchangeably used with “Fe”.

Fig. 5 shows the measured strengths (in Å for atomic features and in magnitude for molecular features) of major indices used in this work for the MaNGA galaxy 1-245451. For purposes of display, the original measured strengths of CN<sub>1</sub> and its error is multiplied by 20 and same is done for Mg<sub>1</sub> but multiplied by 15.

The errors associated with each measurement comes from the variance supplied with the MaNGA DAP data at each pixel. We started off by calculating the Standard Deviation (SD) of the weighted mean flux for both the blue and red continuum separately (continuum are defined in Table 1 for each major index). The SD in each case is square root of the inverse of the sum of inverse variances at each pixel within the continuum (blue or red). The total error from the blue and red continuum is the sum of the errors from both continuum. Next we find the fractional SD at each pixel within the index band from the variance at that pixel. Finally the error in the index strength at each pixel is calculated by using error propagation formulae applied to Equations 2 and 3 of Worthey et al. (1994). The total error is the algebraic sum of errors in each pixel within the index

**Table 1.** The spectral features used in this work. The acronyms are as follows: IB=Index Band, BC=Blue Continuum, RC=Red Continuum. The “Start” and “End” phrases are used to denote the start and end wavelengths of the passbands in Å. The “Unit” column specifies if the index used is an atomic feature (denoted by 0; units: Å) or a molecular feature (denoted by 1; units: mag).

Variable	Feature	IB Start	IB End	BC Start	BC End	RC Start	RC End	Unit
Age	NaD	5876.875	5909.375	5860.625	5875.625	5922.125	5948.125	0
	H $\beta$	4847.875	4876.625	4827.875	4847.875	4876.625	4891.625	0
	Fe5270	5245.65	5285.65	5233.15	5248.15	5285.65	5318.15	0
	Fe5335	5312.125	5352.125	5304.625	5315.875	5353.375	5363.375	0
[Fe/H]	NaD	5876.875	5909.375	5860.625	5875.625	5922.125	5948.125	0
	C <sub>2</sub> 4668	4634	4720.25	4611.5	4630.25	4742.75	4756.5	0
[Na/R]	NaD	5876.875	5909.375	5860.625	5875.625	5922.125	5948.125	0
[C/R]	C <sub>2</sub> 4668	4634	4720.25	4611.5	4630.25	4742.75	4756.5	0
[N/R]	CN <sub>1</sub>	4142.125	4177.125	4080.125	4117.625	4244.125	4284.125	1
[Mg/R]	Mg <sub>1</sub>	5069.125	5134.125	4895.125	4957.625	5301.125	5366.125	1
	Mg <sub>b</sub>	5160.125	5192.625	5142.625	5161.375	5191.375	5206.375	0



**Figure 5.** The strengths of selected features used in this work along with their respective errors for MaNGA galaxy 1-25451. Values are shown for the 1<sup>st</sup> through 7<sup>th</sup> annulus, inclusive. For graphical scaling, CN<sub>1</sub> is multiplied by 20, and Mg<sub>1</sub> is multiplied by 15.

band. The final result is given as the SD by taking square root of this sum.

### 3.2. Model

Naturally, the results of galactic spectral analysis depend on the stellar population model used. The stellar population model utilized for this work is based on [Worthey et al. \(2014\)](#) (hereafter *Worthey* model) with the foundational framework established by [Worthey \(1994\)](#). These models use stellar evolutionary isochrones combined with a stellar initial mass function (IMF) to estimate the distribution of stars within the log L versus log T<sub>eff</sub> diagram. Fluxes are as-

signed to each star bin, along with empirical estimates of the absorption feature indices.

For any stellar population model three major ingredients are: stellar spectral library, set of isochrones, and initial mass function (IMF). The *Worthey* model is based on different stellar spectral libraries: 1. a variant of [Worthey et al. \(1994\)](#) Lick spectra 2. the MILES spectral library ([Sánchez-Blázquez et al. 2006](#)) 3. the Indo-US library by [Valdes et al. \(2004\)](#) 4. the IRTF spectral library ([Rayner et al. 2003](#)) 5. the ELODIE spectral library ([Prugniel & Soubiran 2001](#)). An index fitting function was used to fit the stellar indices as a function of T<sub>eff</sub>, log(g), and [Fe/H] and the functions are incorporated into the models. [Marigo et al. \(2008\)](#) isochrones were used with element sensitivity added to the isochrones according to [Worthey et al. \(2022\)](#). The results from the index fitting functions was associated with this isochrones adopting a Kroupa IMF ([Kroupa 2001](#)). To generate an integrated-light index strength, the flux and continuum values for each “star” along the isochrone are first calculated, with each star’s contribution weighted according to its number. These weighted values are then summed across the entire isochrone. After the summation, the resulting data is reformulated into a final index value, representing the combined (simple) stellar population’s spectral characteristics. An additional weighted sum is performed for this work. Our model also incorporates [Fe/H]-dependent abundance distribution via the abundance distribution function (ADF) ([Tang et al. 2014](#); [Worthey et al. 2005](#)). This allows us to model metallicity-composite stellar populations, but still with a single burst age. In this work we adopt the ‘normal’ width ADF with FWHM = 0.65 dex from [Tang et al. \(2014\)](#).

With a grid of composite models in hand, an inversion program (COMPFIT, to fit observations with a grid of composite models) was developed to determine the optimal set

of abundance parameters for a specified set of indices. It is an improved version of the inversion code used in [Worthey et al. \(2014\)](#).

Here are a few notes on how to interpret the inverted-model results. The final abundance for each element is listed here as the peak (mode) of the ADF, not any kind of SSP-equivalent abundance. Light elements (C, N, O, Si, Na) are assumed to be related to Fe and  $Z$  in a single ratio for each solution (that is, no trend of  $[\alpha/\text{Fe}]$  with Fe or  $Z$  was assumed). Furthermore, due to the subtlety of the spectra features affected by Si and O, inclusion of these elements gives noisy solutions. Therefore, these two elements were tied to Mg, which strongly affects the spectrum. That is,  $[\text{Mg}/\text{Fe}] = [\text{Si}/\text{Fe}] = [\text{O}/\text{Fe}]$  always. This matters because isochrone temperatures vary with O and Si abundance, and there is a strong O-age degeneracy ([Worthey et al. 2022](#)). Elements not mentioned, such as Ni, Cr, Pd, or U, were similarly tied in lockstep to Fe. In this paper, we refer to these unnamed elements by the symbol ‘R.’ Since, for this paper only, we did not allow Fe to vary on its own, R is equivalent to Fe. For example,  $[\text{Mg}/\text{R}] = [\text{Mg}/\text{Fe}]$ . Helium abundance has a non-adjustable trajectory with  $Z$  determined by the isochrone set. This is out of pragmatic necessity, since He cannot be measured in the galaxies studied here, but should be mentioned since it puts an irreducible systematic error into the results.

## 4. RESULTS

In this section we present the results on the age,  $[\text{Fe}/\text{H}]$ , and C, N, Na, and Mg abundances and their radial gradients. For the scope of this paper, the single-burst-equivalent mean age,  $[\text{Fe}/\text{H}]$ ,  $[\text{C}/\text{R}]$ ,  $[\text{N}/\text{R}]$ ,  $[\text{Na}/\text{R}]$ , and  $[\text{Mg}/\text{R}]$  are collectively referred to as stellar population parameters. We first present the stellar population parameters as a function of  $R/R_e$  till  $R/R_e=0.7$  in §4.1. Average parameters binned in  $\sigma$  are listed in Table 2 and parameters binned by  $[\text{Fe}/\text{H}]$  are presented in Table 3. For both of these tables, the values tabulated are the mean of the values from the  $3^{\text{rd}}$  annulus of galaxies within a specific bin. In §4.2 we present the result on radial gradients in the stellar population parameters.

### 4.1. Stellar Population Parameters

The stellar population parameter values are obtained using COMPFIT as described in §3.2. The errors in the calculated parameter values were quantified by running 50 Monte Carlo (MC) realizations of each annulus (for each galaxy). In this method, we randomly varied the measured, corrected index strengths within a Gaussian envelope of  $0.7\sigma$  for 50 times for each annulus. The factor of 0.7 was adopted to reduce the number of outlying solutions, thus improving reliability in error estimation for some galaxies.

The standard deviation of the MC result was adopted as the error for each parameter estimate for each annulus in each galaxy. Solutions for  $[\text{C}/\text{R}]$ ,  $[\text{N}/\text{R}]$ ,  $[\text{Na}/\text{R}]$ , and  $[\text{Mg}/\text{R}]$  are linearized and without bound, but mean age and  $[\text{Fe}/\text{H}]$  could land near the edges of the model grid, namely  $[\text{Fe}/\text{H}]$  near 0.4 and age near 16 Gyr. For solutions near the grid boundaries, the errors generated by MC were increased in an approximate linear fashion to account for missing solutions past the model grid, up to a factor of two for solutions right on the boundary.

#### 4.1.1. Age

Since mass is proportional to the square of the velocity dispersion but only linear with galaxy size ([Bender et al. 1992](#)),  $\sigma$  is an imperfect but adequate proxy for the mass of the galaxy. Fig. 6 shows how the log of mean age (Gyr) changes with  $\sigma$ . The top panel shows mean age of each annulus (annuli are color coded) plotted against log of  $\sigma$ . The  $\sigma$  values on the x-axis are the middle values of the each  $\sigma$  bin (described in 2). The bottom panel shows the mean age for each of the galaxy at their  $3^{\text{rd}}$  annulus. We are considering the  $3^{\text{rd}}$  annulus to be the representative of the whole galaxy in this scenario; more representative than the nucleus or the noisiest annulus, at least. We observe that there is a tendency of larger galaxies to have older age. The slope of the trendline (red color in bottom panel of Fig. 6) is calculated to be 0.59 dex/log( $\sigma$ ). The errorbars associated with each data point on the top panel of Fig. 6 is the mean of the errors for all galaxies within that  $\sigma$  bin for a particular annulus. On the other hand, for the bottom panel, the errors for each data point is the error associated with  $3^{\text{rd}}$  annulus of each galaxy.

#### 4.1.2. $[\text{Fe}/\text{H}]$

Fig. 7 shows how the  $[\text{Fe}/\text{H}]$  values change with  $\sigma$ . The top panel shows mean of  $[\text{Fe}/\text{H}]$  values within in  $\sigma$  bin for every annulus (color coded). The bottom panel shows the  $[\text{Fe}/\text{H}]$  of the  $3^{\text{rd}}$  annulus for each individual galaxy. The negative slope of the binned graph (top panel of Fig. 7) is apparent from the  $2^{\text{nd}}$   $\sigma$  bin. When analyzed individually, we find a slightly negative slope overall for the  $[\text{Fe}/\text{H}]$  vs log( $\sigma$ ) graph in bottom panel of Fig. 7, though the two-segment character is still visible in the data, with an inflection point at roughly log  $\sigma \approx 2.0$  or  $\sigma \approx 100 \text{ km s}^{-1}$ .

#### 4.1.3. C, N, Na, and Mg

Having looked into the trends of age and  $[\text{Fe}/\text{H}]$  with local velocity dispersion, we now focus on the elemental abundances of C, N, Na, and Mg for the 2417 MaNGA galaxies.

In Fig. 8 the elemental abundances are plotted against log  $\sigma$  for each annulus within each  $\sigma$  bin. The galaxies are grouped according to their velocity dispersion (at the  $3^{\text{rd}}$



**Table 2.** Bins in  $\sigma$  used in this work. For each  $\sigma$  bin, the total number of galaxies in that bin and their population parameters are also tabulated. Note that the values tabulated are mean of values from the  $3^{\text{rd}}$  annulus for the galaxies within the  $\sigma$  bin.

$\log \sigma$ Range (km/s)	N	Mean log age (Gyr)	Mean [Fe/H] (dex)	Mean [C/R] (dex)	Mean [N/R] (dex)	Mean [Na/R] (dex)	Mean [Mg/R] (dex)
[1.6, 2]	340	$0.77 \pm 0.09$	$0.02 \pm 0.04$	$-0.1 \pm 0.02$	$-0.35 \pm 0.03$	$-0.23 \pm 0.03$	$-0.19 \pm 0.02$
[2, 2.2]	626	$0.95 \pm 0.1$	$0.07 \pm 0.03$	$0.00 \pm 0.02$	$-0.27 \pm 0.03$	$-0.09 \pm 0.03$	$-0.1 \pm 0.01$
[2.2, 2.34]	783	$1.03 \pm 0.09$	$0.04 \pm 0.03$	$0.07 \pm 0.02$	$-0.21 \pm 0.03$	$0.01 \pm 0.03$	$-0.04 \pm 0.02$
[2.34, 2.45]	560	$1.09 \pm 0.07$	$0.00 \pm 0.03$	$0.14 \pm 0.02$	$-0.12 \pm 0.03$	$0.04 \pm 0.04$	$0.00 \pm 0.03$
[2.45, 2.53]	108	$1.13 \pm 0.06$	$-0.04 \pm 0.03$	$0.17 \pm 0.04$	$-0.04 \pm 0.05$	$0.1 \pm 0.07$	$0.04 \pm 0.06$

**Table 3.** Bins in [Fe/H] used in this work. For each [Fe/H] bin, the total number of galaxies in that bin and mean population parameters are tabulated. Note that the values tabulated are mean of values from the  $3^{\text{rd}}$  annulus of the galaxies within the [Fe/H] bin.

[Fe/H] Range (dex)	N	Mean [C/R] (dex)	Mean [N/R] (dex)	Mean [Na/R] (dex)	Mean [Mg/R] (dex)
[-0.38, -0.16]	235	$0.03 \pm 0.02$	$-0.19 \pm 0.03$	$-0.08 \pm 0.03$	$-0.05 \pm 0.02$
[-0.15, 0.06]	1388	$0.05 \pm 0.02$	$-0.22 \pm 0.03$	$-0.04 \pm 0.03$	$-0.06 \pm 0.02$
[0.06, 0.28]	743	$0.03 \pm 0.02$	$-0.23 \pm 0.03$	$-0.04 \pm 0.03$	$-0.08 \pm 0.02$
[0.28, 0.5]	51	$-0.02 \pm 0.02$	$-0.33 \pm 0.03$	$-0.11 \pm 0.03$	$-0.12 \pm 0.02$

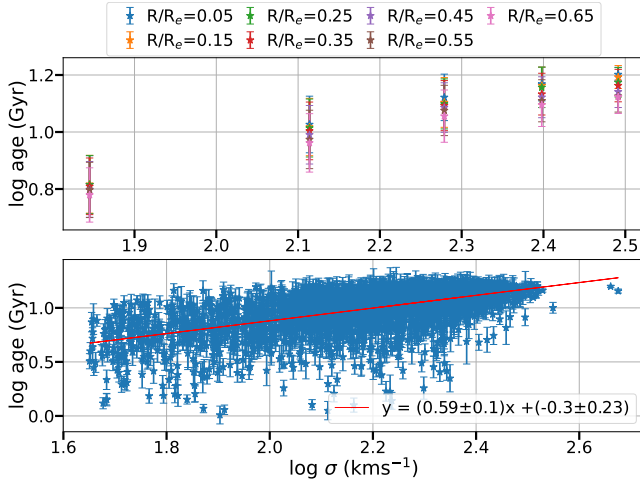


**Figure 6.** The (log of) mean age is plotted against log of  $\sigma$  with errorbars. The top panel shows the mean values for each  $\sigma$  bin ( $\sigma$  bins are described in Table 2) color coded by annulus. The legend on top shows the middle value for each radial bin. The bottom panel shows the mean age of each galaxy's  $3^{\text{rd}}$  annulus. The legend describes the best fit line with 'y' as the mean age and 'x' as the log of  $\sigma$ .

annulus) in accordance to Table 2 and the average abundance values are plotted in Fig. 8. The errorbars come from the taking the average of errors of each measurement within a  $\sigma$  bin for every annulus. Because the light elements are abundant in comparison with Fe-peak elements, it is clear from this figure that the mean abundance increases with increasing  $\sigma$ , even if the Fe abundance by itself does not (Fig. 7). Since  $\sigma$  correlates with galaxy mass,

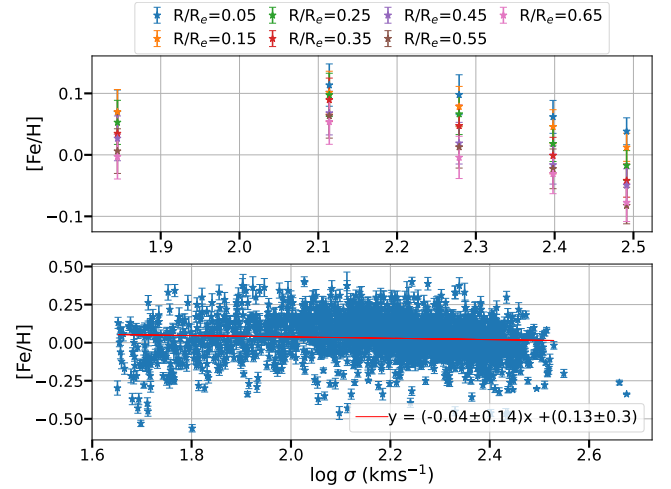


**Figure 7.** Mean [Fe/H] is plotted against log  $\sigma$  with errorbars. The top panel shows the mean values for each  $\sigma$  bin color coded by annulus. The legend on top shows the middle value for each radial bin. The bottom panel shows the mean [Fe/H] of each galaxy for its  $3^{\text{rd}}$  annulus. The legend describes the best fit line with 'y' as the [Fe/H] and 'x' as the log of  $\sigma$ .

it is safe to conclude that massive ETGs have significantly higher abundances of C, N, Na, and Mg.

Note once again that 'R' stands for generic heavy element. While COMPFIT is capable of treating Fe separately from other heavy elements, for the runs that we report on here, Fe has not been allowed to vary by itself, so any [X/R] is equivalent to [X/Fe].

A striking result is obtained, or at least becomes more visible, when we look into elemental abundances at the

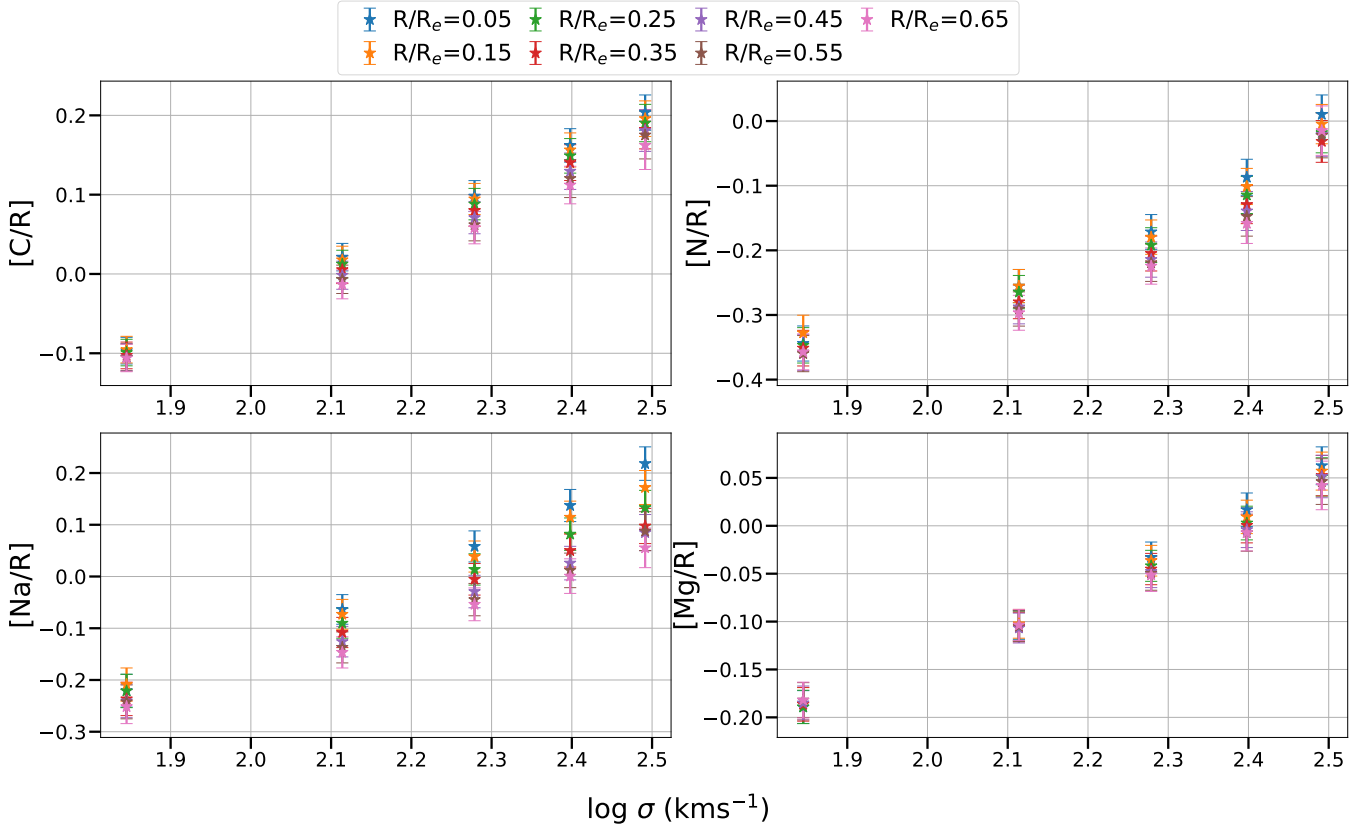


**Figure 8.** The mean elemental abundances for C, N, Na, and Mg plotted against  $\log$  of  $\sigma$ . The annuli are color coded and values are shown in the legend on top of the figure.

individual galaxy level instead of grouping them. In Fig. 9, we find the similar trend of increasing abundance with  $\sigma$  like Fig. 8. But we find a prominent change of slope at  $\log(\sigma)=2.0$  for all the four elements considered in this work. When we compare the slope values from the trend line equations given in Fig. 9, we see that there is an increase in slope by a factor of 2 for C, 6.2 for N, 2.32 for Na, and 1.6 for Mg for  $\log(\sigma)>2.0$ . There is a ‘kink’ at  $\log(\sigma)=2.0$  that mirrors the downward inflection for Fe in Fig. 7. These results point to a suspicion that mid-size to large galaxies might follow different evolutionary paths compared to dwarf elliptical galaxies.

#### 4.1.4. Binned by $[\text{Fe}/\text{H}]$

Apart from investigating the dependence of elemental abundances with  $\sigma$ , we also looked into how they change with  $[\text{Fe}/\text{H}]$ . Errors in  $[\text{Fe}/\text{H}]$  are included in line fits when using  $[\text{Fe}/\text{H}]$  as an independent variable. Due to the smaller relative errors in velocity dispersion, only the errors in the dependent variables were used when performing regressions using  $\sigma$  as the independent variable.

In Fig. 10 we plot the elemental abundances against  $[\text{Fe}/\text{H}]$ . The error bars are again the mean of all the errors of the quantities within each  $[\text{Fe}/\text{H}]$  bin for every  $\sigma$  bin, to represent a typical one-galaxy error. We see an overall

decreasing trend in light elements with increasing  $[\text{Fe}/\text{H}]$ . The lines of slope  $-1$  indicate the trend line if the light element is held constant while Fe alone increases, such as if Type Ia supernovae were the sole contributor. The less-steep falloff of the light elements indicates continued enrichment of lighter elements at higher  $[\text{Fe}/\text{H}]$ . This trend is quantified in Fig. 11 where we plotted elemental abundances of 3<sup>rd</sup> annulus for each galaxy against  $[\text{Fe}/\text{H}]$ . The data is fitted with a linear trend line that has a slightly negative slope for all the elements (see Fig. 11). A zero slope indicates lockstep enrichment with Fe, while a  $-1$  indicates no enrichment. The actual slopes are much nearer to the lockstep case. Romano et al. (2010) charts the behavior of various elements with  $[\text{Fe}/\text{H}]$ . It shows very similar behavior as reported in this work for C, N, Na, and Mg.

The consistency of the results up until this point can be checked by comparing Figures 7, 9, and 11. In Fig. 7 the decreasing trend of  $[\text{Fe}/\text{H}]$  with  $\sigma$  shows that more massive galaxies have lower  $[\text{Fe}/\text{H}]$  and on the other hand Fig. 9 shows that more massive galaxies have higher light metal abundances. So, it is expected that light metal abundances would decrease with increasing  $[\text{Fe}/\text{H}]$ . This trend is confirmed in Fig. 11. The observed change in slope when light metal abundances are plotted with  $\sigma$  vanishes when the

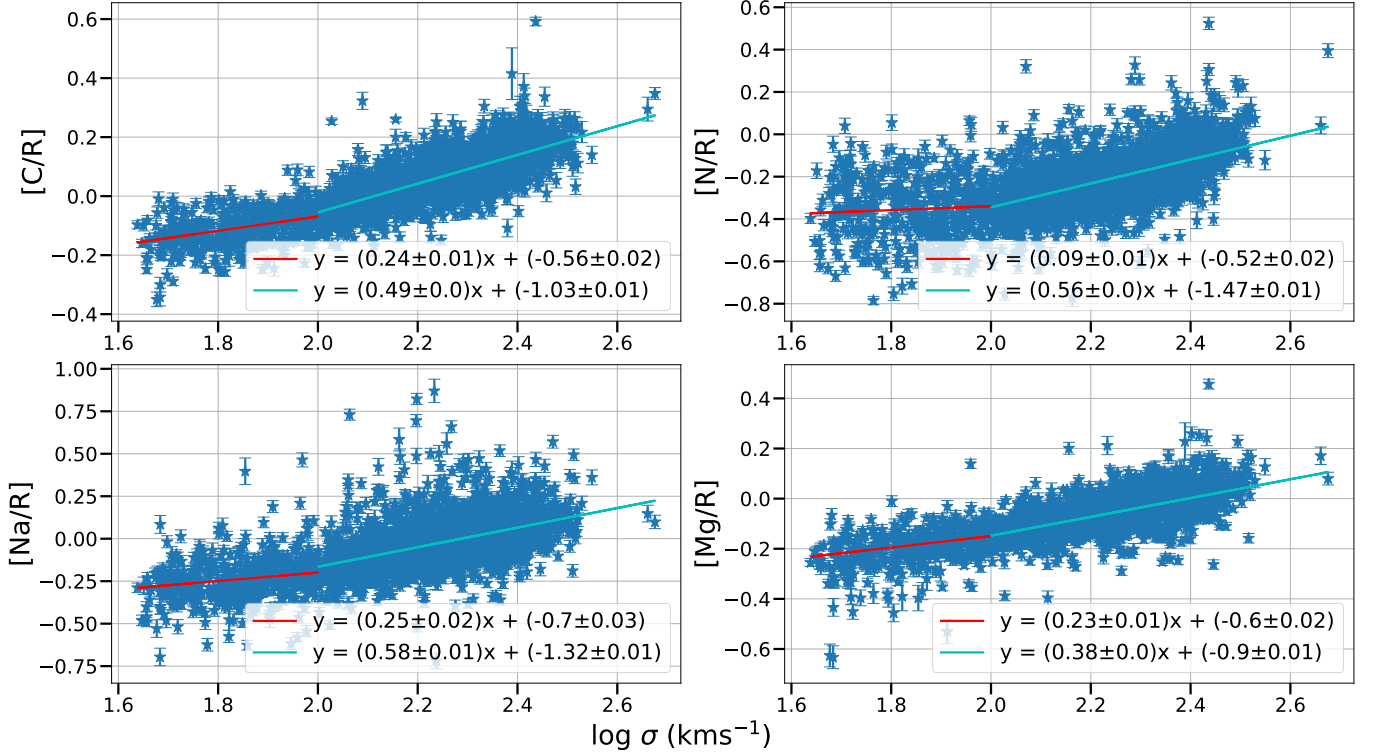


**Figure 9.** The elemental abundances for the 3<sup>rd</sup> annulus of each galaxy are plotted against  $\sigma$ . The error bars come from the 50 Monte Carlo realizations as described in the text. The trendlines show the best fit to the data for  $\log(\sigma) < 2.0$  (in red) and  $\log(\sigma) > 2.0$  (in cyan). The best fit equations are shown as legend with ‘y’ being the elemental abundance and ‘x’ being the  $\log(\sigma)$ .

same quantities are plotted against  $[\text{Fe}/\text{H}]$ , at least for N and Mg. This is an important point to note, as  $\sigma$  reflects galaxy structure, while elemental abundances are indicative of chemical evolution processes.

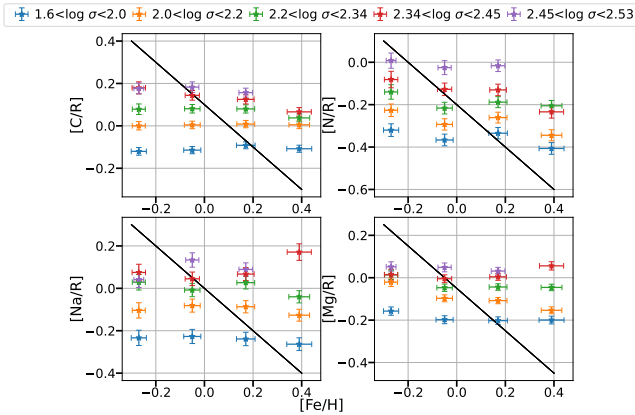


**Figure 10.** Change of light elements' abundance plotted against  $[\text{Fe}/\text{H}]$ . The  $\sigma$  bins are color coded and shown in the legend on top. Note that the galaxies are grouped by  $\sigma$  and  $[\text{Fe}/\text{H}]$  at the 3<sup>rd</sup> annulus. There are no large galaxies for the highest  $\sigma$  and  $[\text{Fe}/\text{H}]$  bin, thus causing absence of data point in the above figure for that bin. Lines of slope -1 (black solid line) indicate the behavior if the light element is held at constant abundance while Fe alone increases.

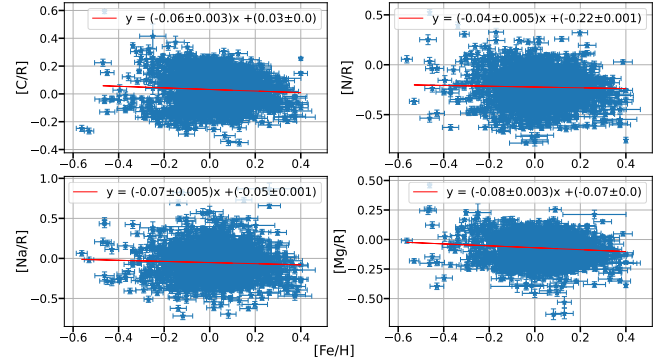


**Figure 11.** Same as Fig. 9 but with  $[\text{Fe}/\text{H}]$  as the independent variable.

In this work we refrained from stacking galaxies together to explore the results at an individual galaxy level. To this end, it seemed interesting to explore how the light element abundances correlate with each other. In Fig. 12 we plotted the abundances of 3<sup>rd</sup> annulus of each galaxy against one another. All the elements positively correlate with each other with C perfectly correlating with Na (as evident by the slope of 1.01 in the trendline equation given in Fig. 12). Fig. 12 also corroborates the fact all the elemental abundances follow similar trend when plotted against both  $\sigma$  (Fig. 9) and  $[\text{Fe}/\text{H}]$  (Fig. 11).

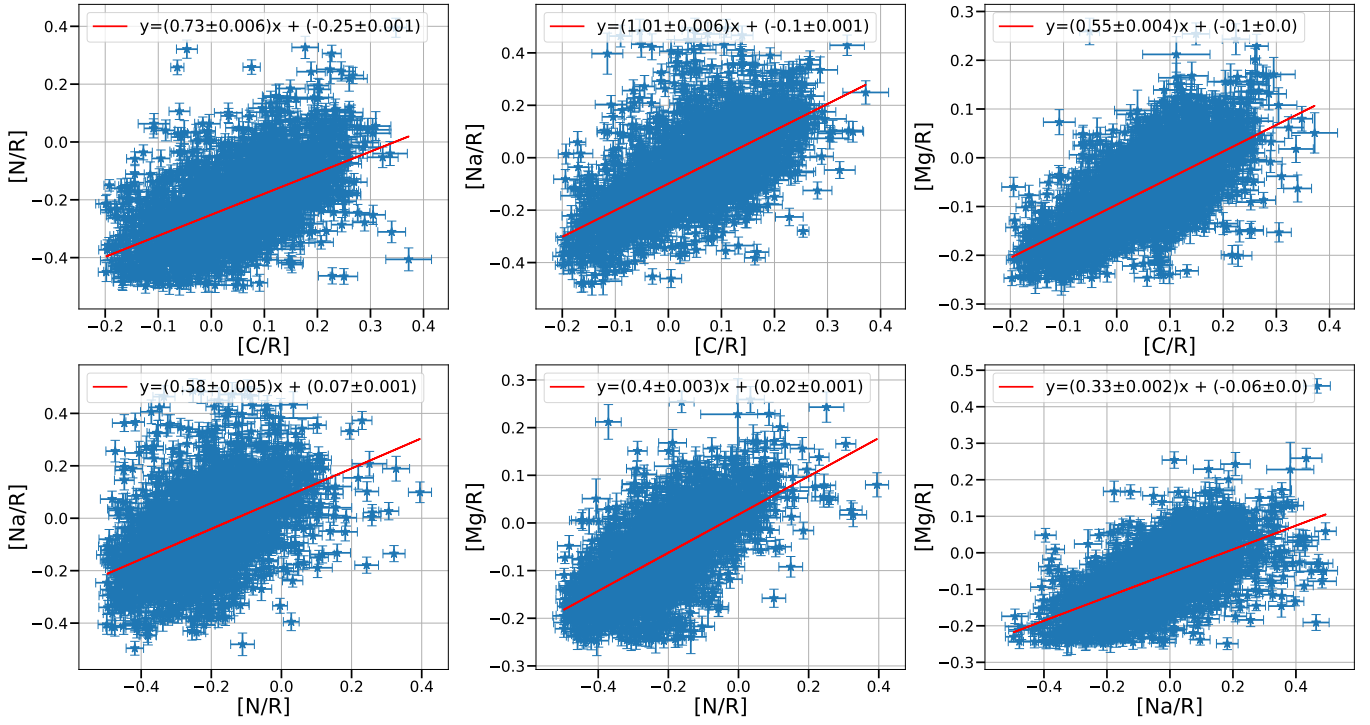


**Figure 12.** The elemental abundances are plotted against each other. The abundances are from 3<sup>rd</sup> annulus of each galaxy. The trendline (in red) equation quantifies their dependence on each other.

#### 4.2. Gradients in Stellar Population Parameters

In this section we describe our radial gradient results. The radial gradients are calculated in log space by dividing the quantity ( $\log(\text{age})$ ,  $[\text{Fe}/\text{H}]$ ,  $[\text{C}/\text{R}]$ ,  $[\text{N}/\text{R}]$ ,  $[\text{Na}/\text{R}]$ , and  $[\text{Mg}/\text{R}]$ ) by  $\log$  of the  $R/R_e$  value. So, the gradient signifies change in any of the quantities (in log scale) for unit change in  $\log(R/R_e)$ . The error in radial gradient is calculated from the covariance matrix between the two quantities. Table 4 shows our  $\sigma$  binning information along with the mean radial gradients for each bin for age,  $[\text{Fe}/\text{H}]$ , and C, N, Na, and Mg abundances.

##### 4.2.1. Age gradients

In Fig. 6 we showed how the age is changing with  $\sigma$ . In this section, we concentrate on how radial gradients in age are changing for galaxies within a particular  $\sigma$  bin ( $\sigma$  bins are described in Table 2 or 4). In Fig. 13 we plot the mean age of each  $\sigma$  bin against the  $\log(R/R_e)$  values. The errorbars for each bin comes from the mean of all the errors within that bin. The errorbars are larger in case of age. On average, we find a flat or very small negative radial gradient in age for all  $\sigma$  bins. However, the scatter is large, implying that while many galaxies are younger in the outskirts, nearly as many are younger in the centers. Only the highest  $\sigma$  bin, with the least-secure counting statistics, shows a situation where the clear majority of the galaxies have older-looking centers and younger outskirts.

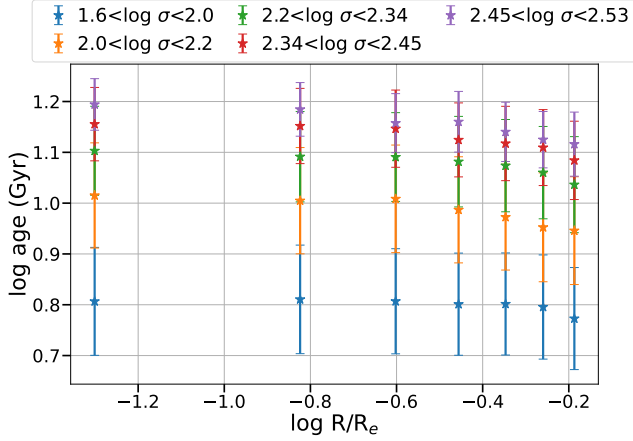
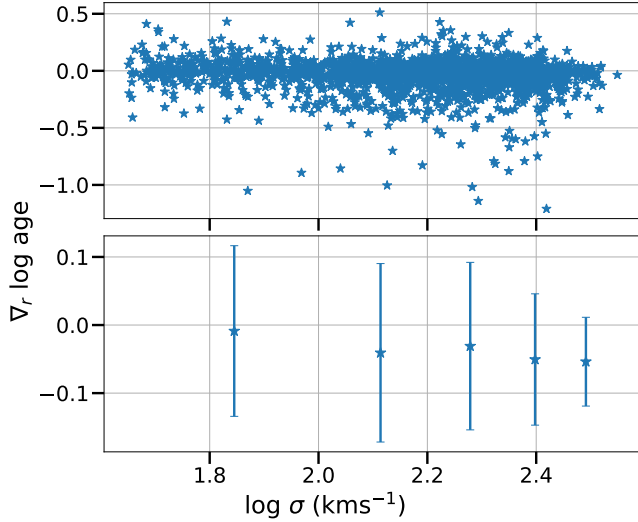
The top panel of Fig. 14 shows the radial gradient values for individual galaxies plotted against  $\sigma$ . The gradient values are predominantly centered near zero. In the bottom panel of Fig. 14 we plotted the mean radial gradient value for each  $\sigma$  bin against the middle value of corresponding  $\sigma$  bin. The least  $\sigma$  bin has near zero mean radial gradient whereas the other  $\sigma$  bins have a near constant value of  $-0.05 \text{ dex}/\log(R/R_e)$ . It should be noted that the gradient error for each bin is not the standard deviation of each bin, but the mean of the radial gradient errors for that bin, which is meant to indicate a typical one-galaxy error.

We need to mention a couple of subtle points as regards Figures 13 and 14. While calculating the mean values in Fig. 13 and bottom panel of Fig. 14, we have omitted outliers using the robust Z-score method. Data points with a Z-score value greater than 3.0 we considered outliers. Small differences arise when comparing the gradients for all the  $\sigma$  bins from Fig. 13 and the radial gradient values shown in the bottom panel of Fig. 14. This is due to methodology. In Fig. 13, we calculate the gradient *after* we calculate mean age (after removing outliers) for each  $\sigma$  bin but in Fig. 14 we first calculate the radial gradient for all galaxies and then calculate the mean. It is generally expected that gradient of the mean will not equal the mean of the gradient. Also, while removing outliers, the methods remove different data points and thus the figures do not produce identical results. These comments are true for Fig. 15 & Fig. 16 pair, and Fig. 17 & figures 18, 19, 20, and 21 pairs.



**Table 4.** Table showing mean radial gradients in  $\log(\text{age})$ ,  $[\text{Fe}/\text{H}]$ , and abundances for C, N, Na, and Mg for each  $\sigma$  bin used in this work.

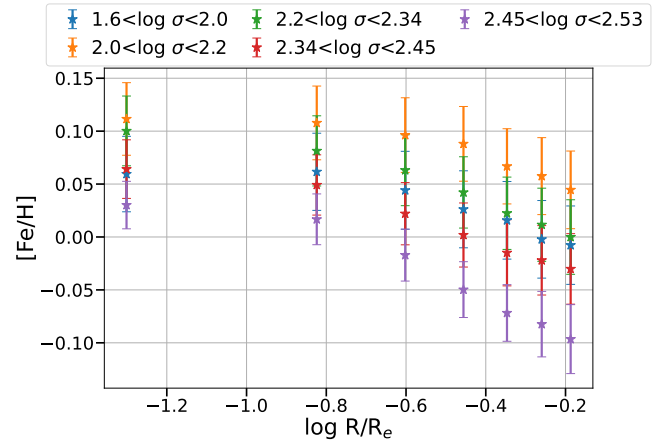
$\log \sigma$ Range (km/s)	N	Mean $\nabla_r \log \text{age}$	Mean $\nabla_r [\text{Fe}/\text{H}]$	Mean $\nabla_r [\text{C}/\text{R}]$	Mean $\nabla_r [\text{N}/\text{R}]$	Mean $\nabla_r [\text{Na}/\text{R}]$	Mean $\nabla_r [\text{Mg}/\text{R}]$
[1.6, 2]	340	$-0.01 \pm 0.13$	$-0.05 \pm 0.05$	$-0.01 \pm 0.02$	$0.00 \pm 0.04$	$-0.02 \pm 0.05$	$0.01 \pm 0.03$
[2, 2.2]	626	$-0.04 \pm 0.14$	$-0.07 \pm 0.05$	$-0.02 \pm 0.02$	$-0.04 \pm 0.03$	$-0.07 \pm 0.04$	$0.00 \pm 0.02$
[2.2, 2.34]	783	$-0.03 \pm 0.12$	$-0.09 \pm 0.05$	$-0.04 \pm 0.03$	$-0.04 \pm 0.04$	$-0.12 \pm 0.04$	$-0.02 \pm 0.02$
[2.34, 2.45]	560	$-0.05 \pm 0.1$	$-0.1 \pm 0.04$	$-0.04 \pm 0.03$	$-0.05 \pm 0.04$	$-0.13 \pm 0.04$	$-0.02 \pm 0.02$
[2.45, 2.53]	108	$-0.06 \pm 0.07$	$-0.12 \pm 0.03$	$-0.03 \pm 0.03$	$-0.04 \pm 0.04$	$-0.15 \pm 0.04$	$-0.03 \pm 0.03$

**Figure 13.** The mean age of each  $\sigma$  bin is plotted against  $\log(R/R_e)$  with errorbars. The legend shows the extent of each  $\sigma$  bin.**Figure 14.** The age gradients for individual galaxy are plotted against  $\sigma$  in the top panel. In the bottom panel, the galaxies are grouped according to their  $\sigma$  (at the 3<sup>rd</sup> annulus) and average age gradient values are plotted against midpoint of the  $\sigma$  bin with errorbars indicating typical error for one galaxy within a  $\sigma$  bin.

#### 4.2.2. $[\text{Fe}/\text{H}]$ gradients

Fig. 15 shows how the mean  $[\text{Fe}/\text{H}]$  for different  $\sigma$  bins (color coded) is changing with radius with  $\log(R/R_e)$  as the

proxy for radius. Qualitatively, a strong negative radial gradient is observed for all  $\sigma$  bins in the sense that very few galaxies show a positive gradient at any bin in  $\sigma$ . Fig. 16 shows the radial gradient values in dex per decade. Individual radial gradients are plotted against corresponding  $\sigma$  values on the top panel of Fig. 16. Similar to §4.2.1, the galaxies are grouped in five  $\sigma$  bins and mean gradient values are plotted against  $\sigma$  in the bottom panel of Fig. 16. The errors are again the mean of individual errors within each  $\sigma$  bin.

**Figure 15.** Same as Fig. 13 but with  $[\text{Fe}/\text{H}]$  on the y-axis.

Compared to §4.2.1, the radial gradients in  $[\text{Fe}/\text{H}]$  have higher negative values and smaller intrinsic scatter (we will shortly show that most of the scatter is astrophysical, not observational in origin). From Fig. 16, the highest  $\sigma$  bin shows a gradient value of  $-0.13$  dex/ $\log(R/R_e)$  which implies that the  $[\text{Fe}/\text{H}]$  drops by 0.13 dex when we move from the innermost annulus to the 5<sup>th</sup> annulus. The fact that the smallest galaxies, which may or may not be merger remnants, have the shallowest  $[\text{Fe}/\text{H}]$  gradients while the largest galaxies, which are definitely shaped primarily by mergers, have the strongest gradients is a point for discussion.

#### 4.2.3. C, N, Na, and Mg gradients

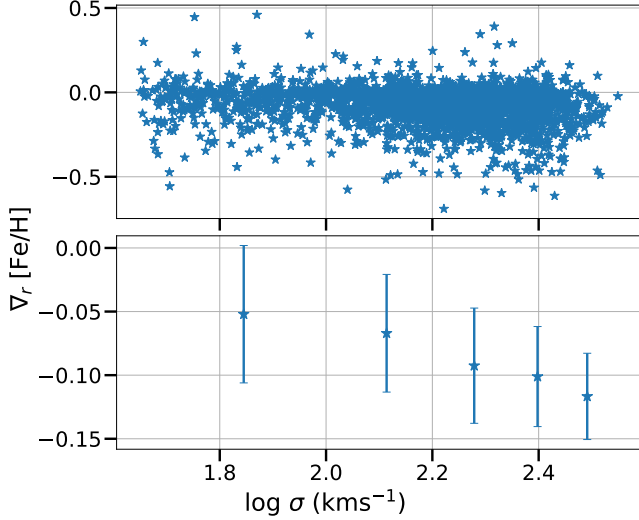


**Figure 16.** Same as Fig. 14 but with  $[\text{Fe}/\text{H}]$  on the y-axis.

Fig. 17 shows how light element abundances are changing with respect to Fe, radially, in five different  $\sigma$  bins. The errorbars associated with each bin is the mean of errors in radial gradient values for the galaxies within that bin. The figure shows once again that the abundances increase with increasing  $\sigma$  value (see also Fig. 8) at all radial values. Na appears to have the highest gradients for all  $\sigma$  values, though due to axis scaling this might most easily be seen in Table 4. Another point worth mentioning here is that not just the abundances, but also the magnitude of the radial gradient steepens with increasing  $\sigma$  value. This implies that more massive galaxies tend to have steeper negative radial gradient in abundances, especially for Na.

Figures 18, 19, 20, and 21 show how the individual radial gradient (top panel) of each galaxy and the mean of radial gradients for each  $\sigma$  bin (bottom panel) changes with  $\sigma$  for C, N, Na, and Mg respectively. The mean values for C, N, and Mg are close to zero for all the  $\sigma$  bins with decreasing trend with  $\sigma$  (the decreasing trend is very prominent for Na and Mg). For Na, there is a strong dependence of the radial gradient value with  $\sigma$ . Not only there is a strong gradient in radial gradient but the absolute values of the radial gradients are also high at higher  $\sigma$  values for Na (Fig. 20). For the highest  $\sigma$  bin in Fig. 20, a negative gradient value of 0.15 signifies that if we move to the 5<sup>th</sup> annulus from the center of the galaxy, there is a drop in Na abundance by 0.15 dex. For Mg, although the higher  $\sigma$  bins have a more negative mean radial gradient value, the absolute values are on the lower side. The low- $\sigma$  galaxies have near-zero gradients in individual light element abundances, though most of them have negative  $[\text{Fe}/\text{H}]$  gradients.

Since we are treating each galaxy as an individual entity in this work, we wanted to look into how the radial gradient values in these four elements correlate with each other

(if there is any correlation at all). In order to check any such correlation, we plotted the individual radial gradients in different elements with each other and calculated the Spearman correlation. A positive Spearman coefficient signifies a positive correlation with values closer to one meaning very high positive correlation, whereas a negative value indicates a anti-correlation with values close to negative one signifying the most anti-correlation.

Fig. 22 shows the plots of radial gradients in C, N, Na, and Mg plotted against each other for all possible combinations of these four elements. The radial gradients in C and Na seem to correlate the most ( $\rho=0.36$ ) compared to others. But a low  $\rho$  value signifies little positive correlation. Mg has a very similar correlation ( $\rho \sim 0.3$ ) with all the rest of the elements (C, N, and Na). N and C are the least correlated pair among all of them with a  $\rho$  value of 0.13, this is almost equivalent to having no correlation (signified by a  $\rho$  value near zero). Na and N have the second least correlation value at  $\rho=0.21$ .

## 5. DISCUSSION

In this work, we derived the stellar population parameters (age,  $[\text{Fe}/\text{H}]$ ,  $[\text{C}/\text{R}]$ ,  $[\text{N}/\text{R}]$ ,  $[\text{Na}/\text{R}]$ , and  $[\text{Mg}/\text{R}]$ ) and their radial gradients for 2417 individual MaNGA galaxies at different radial distances from the center of the galaxy. In §4.1, we show how different stellar population parameters are changing with  $\sigma$  and  $[\text{Fe}/\text{H}]$  whereas in §4.2, we illustrate the dependence of radial gradients on  $\sigma$ . In this section we compare some of our key results with previous work and also provide a broader implication of this work in terms of galaxy formation and evolution.

### 5.1. Stellar Population Parameters

Fig. 6 shows how the individual age of galaxy (for the 3<sup>rd</sup> annulus; bottom panel) and mean age (within each  $\sigma$  bin; top panel) changes with  $\sigma$ . We see a positive correlation between the two with the age steadily increasing with the size of the galaxy. This is also evident from the positive slope of 0.59 in the bottom panel of Fig. 6. This slope is in good agreement with Parikh et al. (2019) (their Fig. 7) and Worthey et al. (2014) (their Fig. 3). Although Worthey et al. (2014) does not provide with a trendline fit to the data, the extent of the age at two ends of  $\sigma$  is similar to that of our result. Conroy et al. (2014)'s Fig. 18 shows variation of different parameters with  $\sigma$  with a gradient of around 0.55 for  $\log(\text{age})$  vs  $\log(\sigma)$  relationship. This difference in the gradient (compared to our 0.59) rises probably because of difference in stellar population models used for these two works. Johansson et al. (2012) reports a gradient value of 0.73 for their  $\log(\text{age})$  vs  $\log(\sigma)$  relationship for around 4000 SDSS ETGs. Within the scope of errors, we also reproduced similar results as Johansson et al. (2012) with our individual MaNGA galaxies. These various good agreements

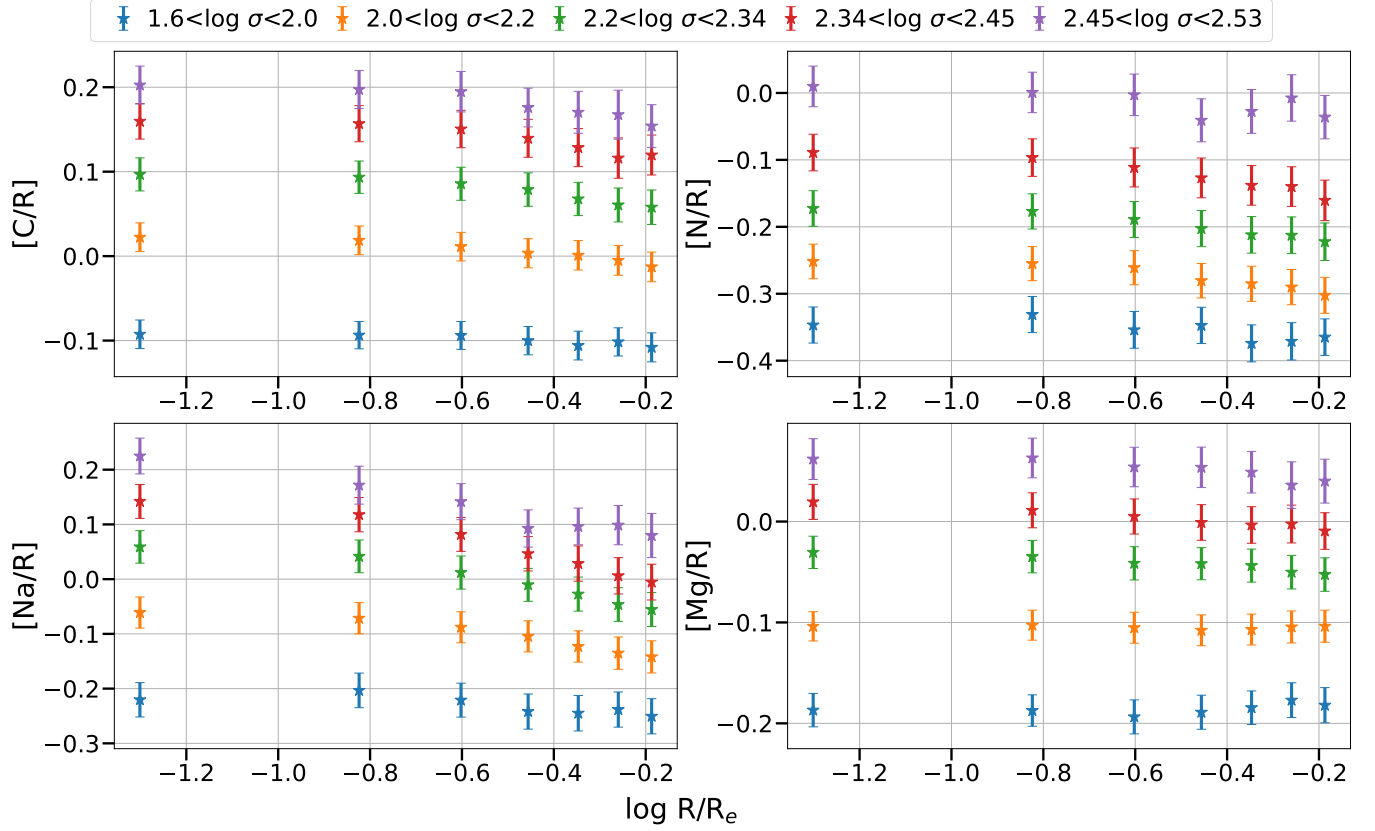


**Figure 17.** The abundance of all the elements are plotted against  $\log(R/R_e)$ . The galaxies are grouped according to their  $\sigma$  values in five different  $\sigma$  bins (color coded) with errorbars. The legend lists the extent of each  $\sigma$  bin, following Table 2.

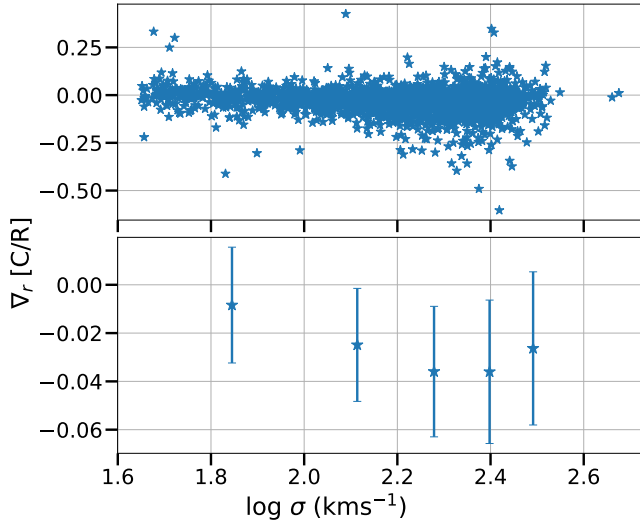


**Figure 18.** The top panel shows the calculated radial gradients in C plotted against  $\sigma$  for all the galaxies. The bottom panel shows the mean gradient value for each  $\sigma$  bin. The errorbars in the bottom panel comes from the mean errors in radial gradient for all the galaxies within a certain  $\sigma$  bin. Errorbars are not shown on the top panel in order to avoid crowding in the figure.

are interesting because of the volatile oxygen-age degeneracy [Worthey et al. \(2022\)](#) along with our assumption that

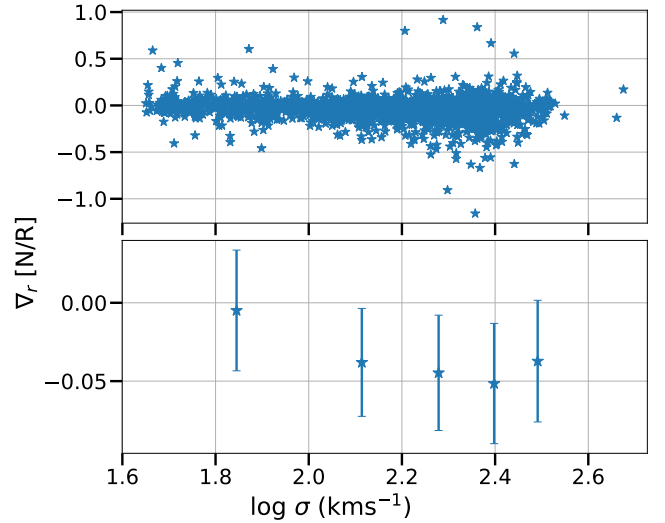


**Figure 19.** Same as Fig. 18 but for N.

$[Mg/R] = [O/R]$ ; with such a large increase in model flexibility, there was no *a priori* reason that the age scale would remain unchanged. This trend of larger galaxies having older age is valid irrespective of the density of environment according to [Thomas et al. \(2005\)](#). These considerations support an anti-hierarchical picture where larger (more mas-

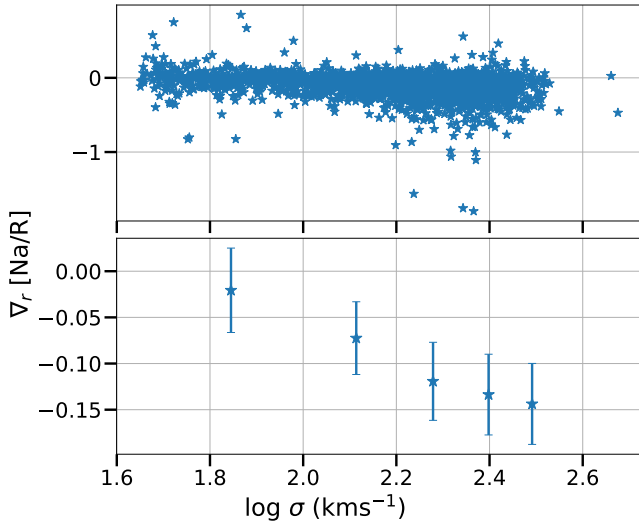


Figure 20. Same as Fig. 18 but for Na.

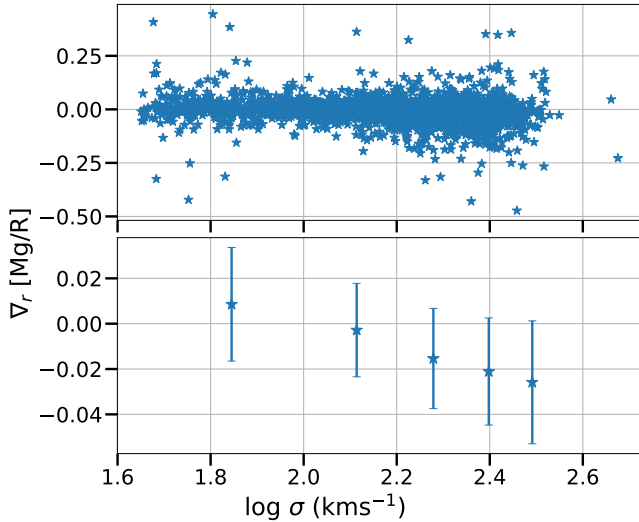


Figure 21. Same as Fig. 18 but for Mg.

sive) ETGs were formed at an earlier stage of the evolution of the Universe.

Shifting our focus to  $[\text{Fe}/\text{H}]$ , Fig. 7 showed how  $[\text{Fe}/\text{H}]$  varies as a function of  $\sigma$  for both individual galaxies (3<sup>rd</sup> annulus; bottom panel) and  $\sigma$  bins (top panel). In conjunction with Fig. 6, we can also conclude that older galaxies tend to have slightly lower  $[\text{Fe}/\text{H}]$ . We emphasize again that due to innovations in our modeling (isochrones that shift in temperature for individual elements and metallicity-composite base models) our results should not necessarily track previously published results. That said, a similar trend is also found in Trager et al. (2000b) where for a given  $\sigma$ , older galaxies are found to have low  $[\text{Fe}/\text{H}]$ . Although the opposite trend is shown in some papers (Conroy et al. 2014), many studies show a similar flat to negative depen-

dence on  $[\text{Fe}/\text{H}]$  when plotted against  $\sigma$  (Johansson et al. 2012). This behavior can be attributed to several factors.

One possible driving factor in reduced  $[\text{Fe}/\text{H}]$  in galaxies is high star formation rate (SFR) of the galaxy (Lara-López et al. 2010). Davé (2008) have shown that galaxies with higher stellar mass tend to have higher SFR within a redshift ( $z$ ) range of 0-2. The higher SFR also produces stronger outflows within a galaxy that further reduces its  $[\text{Fe}/\text{H}]$  (Cicone et al. 2016). Perhaps, high  $\sigma$  galaxies tend to have a higher SFR and stronger winds that lead to slightly lower  $[\text{Fe}/\text{H}]$  compared to low  $\sigma$  galaxies, yielding a slightly negative trend in Fig. 7. These high  $\sigma$  galaxies have higher light element abundances (Fig. 8), but one could posit that the time delay between Type II supernova enrichment and delayed Type Ia supernova enrichment makes enriched gas produced by the latter more susceptible to ejection by galactic winds.

In Fig. 8 we see a trend of increasing abundance for all elements explored in this work (C, N, Na, and Mg). Previous work on elemental abundances in ETGs shows a very similar trend (Parikh et al. 2021; Johansson et al. 2012; Conroy et al. 2014; Graves et al. 2007). Apart from Mg, none of the elements explored in this work can be termed as  $\alpha$  elements. Each of them have different pathways of formation.

Nitrogen is expelled from supernova explosions, but is mostly formed through the CNO cycle in stars from carbon. Some carbon is also produced by supernovae, but most comes from the triple alpha process. For both elements, stellar winds during the late stages of evolution enrich the nearby interstellar medium. For stellar populations, carbon production is dominant in stars with lower mass (1-3  $M_{\odot}$ ) whereas for nitrogen we need higher mass stars (4-8  $M_{\odot}$ ) (Chiappini et al. 2003). In Milky Way stars,  $[\text{C}/\text{Fe}]$  hovers near zero as a function of  $[\text{Fe}/\text{H}]$ , while  $[\text{N}/\text{Fe}]$  rises with metallicity (Jönsson et al. 2018). In this work, we see that N is under-abundant (on average by 0.25 dex) compared to C, and compared always to the solar ratio. Conroy et al. (2014) reported similar abundance values and gradient for C and N.

Not included in the models explicitly is the effect of first dredge-up on the first-ascent red giant branch. Nitrogen abundance increases by  $\sim 0.4$  dex relative to C on the upper RGB [see, e.g., Fig 2 of Martig et al. (2016)]. If this effect were included, nitrogen's spectral signatures would strengthen and the inferred N abundance would drop even lower in Fig. 12, putting  $[\text{N}/\text{C}]$  and  $[\text{N}/\text{Fe}]$  significantly low compared to the Milky Way. The effect is included implicitly, in that Milky Way stars were used to empirically zero the spectral library, and this effect is built in, masking as a surface gravity effect. That said, and keeping also in mind the N-rich globular cluster system in M31 that contrasts so strongly with our own cluster system (Worthey



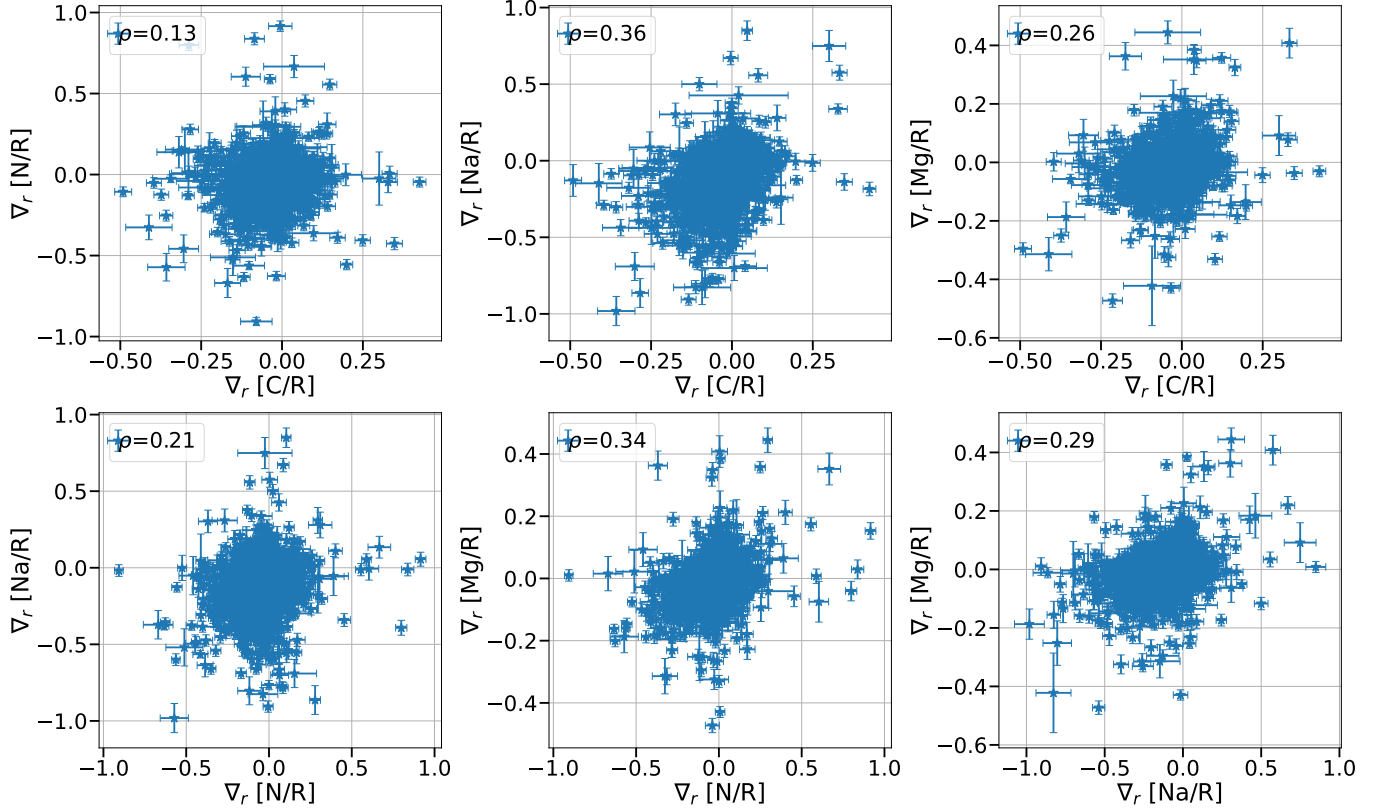


**Figure 22.** The radial gradient values in C, N, Na, and Mg for each individual galaxy are plotted against one another. The legend shows the Spearman coefficient value for each combination of elements. The errorbars are added for each data point as well.

1998) and the small dynamic range of current galaxy formation model predictions (Fig. 31), it is safe to say that N is telling us much about chemical evolution that we are not yet equipped to interpret.

We see very similar abundances trajectories for sodium and magnesium (see Fig. 8). Although these two elements have different nucleosynthetic origins, both Na and Mg are mostly sourced from type II supernova (SNII) explosions (Marigo 2001; Trager et al. 2000a) with significant contributions from the  $\alpha$ -rich freezeout phase of the explosion (Woosley & Weaver 1995), so their nucleosynthetic origin *site* is similar. The ‘locked-in’ state of ETGs in terms of chemical abundances preserve this signature of Na and Mg over time.

A remarkable finding from this work is shown in Fig. 9. The effect shows more clearly because we did not stack spectra. What we see is that there is a very prominent increase in slope of chemical abundances when plotted against  $\sigma$  for  $\log(\sigma) > 2.0$ . This slope change seems not to have been mentioned in previous literature on this subject. Possibly related, however, is that Gallazzi et al. (2005) found a transition from low mass to massive galaxies in the mass-metallicity relation at around  $\log(\sigma) = 2.3$ . Evidently, low mass galaxies are less efficient in producing light metals and retaining them compared to massive galaxies. Dif-

ferent factors could lead to this, including star formation efficiency, galactic winds, and the IMF.

Figs. 10 (grouped according to annulus) and 11 (3<sup>rd</sup> annulus for each galaxy) show the dependence of the elemental abundances with  $[\text{Fe}/\text{H}]$ . For all the elements, we see a slight negative trend i.e. with increasing  $[\text{Fe}/\text{H}]$  the elemental abundances specifically light metal abundances decrease. The trend in ETGs resembles the Milky Way trend only for Mg. The  $[\text{C}/\text{R}]$ ,  $[\text{N}/\text{R}]$ , and  $[\text{Na}/\text{R}]$  trends are qualitatively different. Timmes et al. (1995) simulate evolution of 76 stable isotopes in galaxies. Their work (and references therein) shows that both carbon and nitrogen remain constant over a large range of  $[\text{Fe}/\text{H}]$  whereas sodium and magnesium steadily decrease with increasing  $[\text{Fe}/\text{H}]$ . Other than nitrogen (which is depleted by a factor of 0.2 dex on an average compared to solar), we report very near solar abundance for the rest of the elements. The decreasing trend of light metal abundances with  $[\text{Fe}/\text{H}]$  is a complicated phenomenon to explain, but surely must be tied to the fact that the iron production comes in large part from type Ia supernova explosions (SNIa). Additional Fe reduces the  $[\text{X}/\text{Fe}]$  ratio while enhancing the  $[\text{Fe}/\text{H}]$  value. For magnesium, Sybilska et al. (2018) and Conroy & van Dokkum (2012) report a generic decrease in  $[\text{Mg}/\text{Fe}]$  value with increasing  $[\text{Fe}/\text{H}]$ . The simulation results from Alibés et al.

(2001) also agree very well with our findings. It is to be noted that our results for Na, do not agree with the results presented in Parikh et al. (2021).

### 5.2. Radial Gradients in Stellar Population Parameters

The radial gradients in different stellar population parameters provide insight into the formation and evolution of galaxies. In this work, in addition to looking at the trends of stellar population parameters with  $\sigma$ , we also investigate their radial gradients and their trends with  $\sigma$ .

In Fig. 13 we show how the mean age for each  $\sigma$  bin changes radially from the center of the galaxy to  $0.7 R_e$ . We find a somewhat shallow decreasing trend of mean age with radius on average, but the scatter is much larger than the mean trend. This result is also validated through Fig. 14. There are studies that report nearly zero radial gradient in age (Mehlert et al. 2003; Sánchez-Blázquez et al. 2007; Kuntschner et al. 2010). Some other studies show negative mean radial gradient in age (Rawle et al. 2008, 2010; Parikh et al. 2021). Our result, showing a modest radial gradient in age, is consistent with these results within the scope of error. Most of the previous studies on radial gradient in age consider ages out to  $R=R_e$ , but in this work we calculated spatial information to  $R=0.7 R_e$ . A lack of age gradient might imply that stellar populations in ETGs were formed in bursts that spanned large swaths of galactocentric radius. In other words, star formation tends to be global, not outside-in or inside-out. However, it needs to be remembered that our results apply to the average. Few galaxies conform to the average. Slightly more than half are younger in the outskirts ( $0.7 R_e$  for this study) and slightly less than half are younger in the center. Only a minority of galactic accretion events drive gas to galaxy centers, it seems.

We find radial gradients in  $[\text{Fe}/\text{H}] \approx -0.10$  [dex per decade,  $[\text{Fe}/\text{H}]/\log(R/R_e)$ ] for the middle  $\sigma$  bin with substantial dependence on  $\sigma$  (see Fig. 16). This value is very similar to values reported by Parikh et al. (2021) and Mehlert et al. (2003) but of shallower slope than some other works (Kobayashi 2004; Kuntschner et al. 2010). Earlier estimates averaged a slope of  $-0.2$  dex per decade for medium and large ETGs (Henry & Worthey 1999). We see a considerable scatter around zero (see top panel of Fig. 16) with values as negative as  $-0.5$   $[\text{Fe}/\text{H}]/\log(R/R_e)$  and as positive as  $0.25$   $[\text{Fe}/\text{H}]/\log(R/R_e)$  (not considering outliers). Our trend of radial  $[\text{Fe}/\text{H}]$  gradient with  $\sigma$  qualitatively matches with Spolaor et al. (2009) at low  $\sigma$  values ( $\log(\sigma) < 2.0$ ) and with Bekki & Shioya (1999) for higher  $\sigma$  values. A negative  $[\text{Fe}/\text{H}]$  gradient favors an ‘inside-out’ mode of chemical evolution in ETGs if star formation and enrichment occur on a timescale similar to the accretion itself. This conclusion is similar to that of Goddard et al. (2017) where they find similar results with 505

ETGs. The  $[\text{Fe}/\text{H}]$  radial gradient reported here could also be explained as a consequence of hierarchical merging events. If they involve gas, mergers can trigger intense central starbursts, which significantly enrich the core regions with metals leading to a metallicity distribution where the central areas exhibit higher metal content than the outer regions (Kobayashi 2004). If not subsumed into star formation right away, gas loses energy and angular momentum, funneling into the central regions where concentrated star formation enriches the core with metals more significantly than the outskirts (Montes et al. 2014). The gradual increase of  $[\text{Fe}/\text{H}]$  radial gradient with  $\sigma$  can also be explained by the amplification of these processes for larger galaxies. The monolithic collapse hypothesis on the other hand predicts a much higher  $[\text{Fe}/\text{H}]$  gradient (Kawata 2001; Pipino et al. 2010) than what is reported here. If monolithic collapses are a common formation channel, then we also require major “dry” merger events to explain the much flatter slope in  $[\text{Fe}/\text{H}]$ .

Using a linear scale for  $R/R_e$ , the negative radial gradient in age is  $0.04$  dex per  $R/R_e$  for the lowest  $\sigma$  bin and remains constant at an increased value of  $0.11$  dex per  $R/R_e$  for the rest of the  $\sigma$  bins. We quantify the goodness of fit for both logarithmic and linear cases using the coefficient of determination aka the  $R^2$  value. The  $R^2$  values for each  $\sigma$  bin for the linear case are (in order of increasing  $\sigma$ ): 0.52, 0.93, 0.97, 0.94, and 0.95. On the other hand, for the logarithmic case, the  $R^2$  values are: 0.26, 0.70, 0.77, 0.71, 0.85. Thus, in general, the linear case shows better fit. Similar analyses were also performed for the radial gradients in  $[\text{Fe}/\text{H}]$ . The negative radial gradient in  $[\text{Fe}/\text{H}]$  (using linear scale for  $R/R_e$ ) increases from  $0.12$  dex per  $R/R_e$  to  $0.23$  dex per  $R/R_e$  with  $R^2$  values of 0.96, 0.97, 0.97, 0.98, and 0.98 for different  $\sigma$  bins (in order of increasing  $\sigma$ ). Using the logarithmic scale the  $R^2$  values are 0.79, 0.81, 0.91, 0.93, and 0.84, again showing better fit for the linear case. Thus for both age and  $[\text{Fe}/\text{H}]$  we find that a linear physical scale in kpc connects to the spatial dependencies of chemical evolution better than a logarithmic one. For example, this might mean that power-law dependencies such as depth of potential well or dynamical crossing time are less important than turbulence or other processes with a relatively fixed sphere of influence.

Fig. 17 shows the radial trend of all of the elements explored in this work. Below we’ll discuss each of the elements individually.

Carbon (C) and nitrogen (N) are not considered  $\alpha$  elements, but they follow the same qualitative trend as Mg. Radial gradients (as a function of  $\sigma$ ) for C and N are shown for all the  $\sigma$  bins in Figures 18 and 19 respectively. One notable feature in both of these figures is that for massive ETGs ( $\log(\sigma) > 2.0$ ) the radial gradients in C and N seem to

have flattened with  $\sigma$  on average, although the gradient amplitude is very small for these elements. Parikh et al. (2021) reported a very flat gradient for both of these elements for almost all of their mass bins. Feldmeier-Krause et al. (2021) reported a very flat gradient for C but slightly negative gradient for N. Within the errors, our results agree with these studies. Additionally, Feldmeier-Krause et al. (2021) found no significant correlation between radial gradients in C and N with  $[\text{Fe}/\text{H}]$ , which we also did not find (figure not shown in this article).

The strongest gradient values are obtained for sodium. Fig. 20 shows that the negative radial gradient in Na increases monotonically with  $\sigma$ . The median negative gradient of around 0.10  $[\text{Na}/\text{Fe}]/\log(R/R_e)$  in this work is similar to a number of previously reported values La Barbera et al. (2017); Parikh et al. (2021). Feldmeier-Krause et al. (2021) reports strong negative radial gradient in  $[\text{Na}/\text{R}]$  for individual ETGs, but their  $[\text{Na}/\text{R}]$  values are higher than what we report in this work. Given the overall similarity between Mg and Na trends *among* ETGs, the  $\sim 2$  times stronger Na gradients *within* ETGs are puzzling.

Magnesium (Mg) is considered an  $\alpha$ -element that is predominantly produced inside massive stars via fusion of helium nuclei. In this work, Mg shows negative radial gradient for all  $\sigma$  bins (qualitatively in Fig 17 and quantitatively in Fig. 21). Early work by Davies et al. (1993) showed that the radial gradient in the  $\text{Mg}_2$  index has a value of around -0.06 which can be translated roughly to a radial gradient in  $[\text{Mg}/\text{R}]$ . Our highest  $\sigma$  bin has a mean radial gradient value of around -0.02  $[\text{Mg}/\text{R}]/\log(R/R_e)$  and gradually decreases to a flat gradient for the lowest  $\sigma$  bin. Many previous studies reported a radial gradient value of near -0.06 (Rawle et al. 2008; Ferreras et al. 2019; Feldmeier-Krause et al. 2021), whereas Mehlert et al. (2003) and Parikh et al. (2021) report zero radial gradient for  $[\text{Mg}/\text{R}]$ . In the average ETG, if there is such a thing, the Mg abundance is global; independent of radial distances from the center of the galaxy.

### 5.3. Scatter in Astrophysical Parameters and their Radial Gradients

Once observational effects are subtracted, the scatter of a derived quantity within a group of galaxies reveals the extent of variation within the population allowed by natural evolutionary pathways. With over 2000 galaxies, sample size should not be a concern, and the extent of natural variation should be well-measured. In this section we show results of our calculated intrinsic scatter ( $\delta_i$ ) and how they correlate with  $\sigma$ . In general, we find that observational errors are small enough that almost all of the scatter in previous figures comes from the intrinsic scatter.

Intrinsic scatter ( $\delta_i$ ) is calculated via

$$\delta_T^2 = \delta_i^2 + \delta_o^2, \quad (3)$$

where  $\delta_T$  is the total scatter in a derived quantity and  $\delta_o$  is the variation in that quantity given the observational scatter.  $\delta_T$  for each  $\sigma$  bin is the standard deviation in the astrophysical parameter or radial gradient within that  $\sigma$  bin.

The best way to estimate  $\delta_o$  is via repeated observations of the same target, which MaNGA does not provide. However, MaNGA does calculate the uncertainty per spectral pixel, and this is readily translated to uncertainty per measured index value. We assume that spectral response ripples over spectral scales of 10Å to 100Å, which can be a significant error source for some spectrographs, are not a significant source of error for MaNGA. Our method to estimate  $\delta_o$  is to randomly vary each index measurement within its Gaussian probability distribution, and then recalculate COMFIT solutions. The as-measured solution was taken as the mean, then 50 variations for each annulus were generated. This provided us with a proxy for standard deviation for each measurement. To obtain an equivalent error for the radial gradient measurements, we used the error from the covariance matrix that was generated while calculating the radial gradients.

To get to  $\delta_o$  from the errors from MC realizations or gradient errors, we use

$$\delta_o = \sqrt{\frac{1}{\sum_{i=1}^N \Delta_i^{-2}}} \times \sqrt{N}, \quad (4)$$

where  $\Delta_i$  is the error from MC realizations or gradient errors for a particular galaxy's measurement within a  $\sigma$  bin and  $N$  is the total number of galaxies within that same  $\sigma$  bin. Armed with these formulae we calculated the  $\delta_i$  for the age,  $[\text{Fe} / \text{H}]$ , C, N, Na, and Mg estimates and their radial gradients for each  $\sigma$  bin.

In Fig. 23 we show the calculated  $\delta_i$  for the age and radial gradient in age. We see a constant decreasing trend for  $\delta_i$  in age with  $\sigma$  and  $\delta_i$  for the highest  $\sigma$  bin (0.05 dex) is four times less than for the lowest  $\sigma$  bin (0.2 dex). The  $\delta_i$  in radial gradient trends the opposite way, with the flat gradients in low- $\sigma$  galaxies showing little scatter, while the almost-flat age gradients in high- $\sigma$  galaxies show large intrinsic scatter that straddles zero.

The slightly contradictory observation that the most age-homogeneous galaxies also have the most astrophysical spread in age gradient actually fits well with the scenario where the more massive galaxies are formed by large number of merger events compared to smaller galaxies which are considered to have gone through less number of merger events. Faber et al. (2007) showed that number of red galaxies (ETGs) have been significantly rising from  $z \sim 1$  to the present day ( $z=0$ ). In order to explain

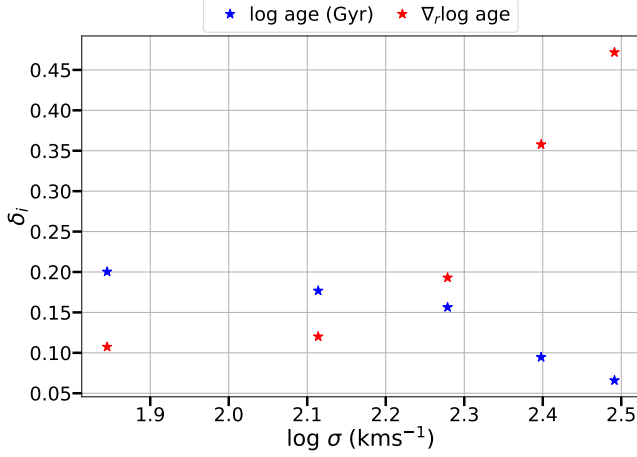


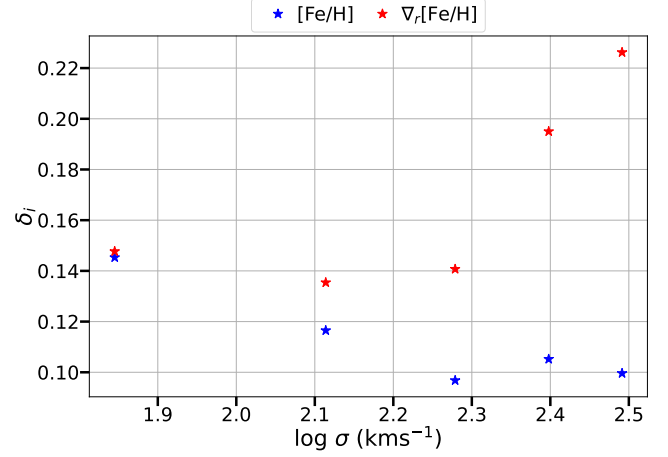
**Figure 23.** The intrinsic scatter ( $\delta_i$ ) in age (blue) and in radial age gradient (red) plotted against  $\sigma$ . The unit associated with age is dex and that with radial gradient is dex/log( $R/R_e$ ).

this scenario, the authors posit that migration of galaxies to the red sequence is caused by both quenching and merger events. We also support a more homogeneous age distribution for galaxies with high  $\sigma$ . In a merger-dominated scenario, the placement of youthful stars post-merger (nearer to the center or nearer to the edges) seems dependent on gas content, kinematic initial conditions, and the ages of the merger components. That is, we see no contradiction that increased merging causes larger scatter in age gradient.

At the low- $\sigma$  end, if these galaxies are objects that escaped becoming incorporated into larger units, they are missing an important quenching mechanism (merging) and therefore might be expected to have a large scatter in mean age, as we observe.

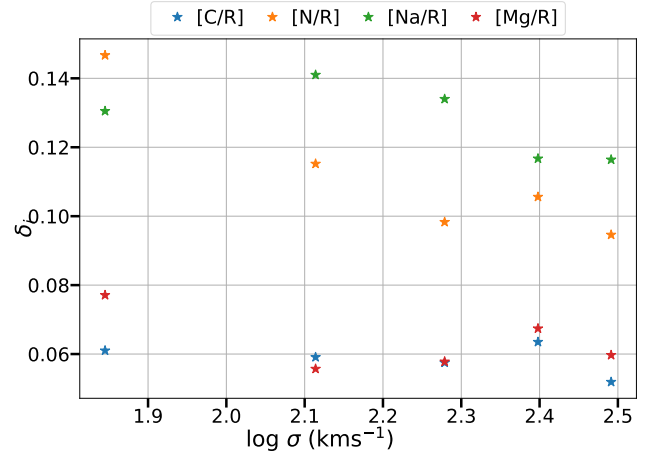
Some galaxy formation scenarios posit that a gas collapse forms strong abundance gradients in galaxy subunits, many of which later merge and therefore lessen the gradients. These scenarios predict the weakest gradients should be seen in high- $\sigma$  galaxies. If gas is involved in the mergers, high- $\sigma$  galaxies should also show the highest abundances and youngest ages. None of these predictions are consistent with our results. A comparison with IllustrisTNG hierarchical simulations, on the other hand, reproduce the age structure we find, show the abundance slope changes at  $\log(\sigma) \approx 2.0$  that we observe, and exhibit flat gradients similar to those we derive, although the abundances predicted by IllustrisTNG are significantly higher than our observations overall. The Illustris comparison is discussed below in section 5.4.

Fig. 24 shows the variation of  $\delta_i$  in [Fe/H] and corresponding radial gradients for all of our defined  $\sigma$  bins. As with mean age, a decreasing trend of  $\delta_i$  in [Fe/H] can be seen with increasing  $\sigma$ , paired with an increase of variation



**Figure 24.** The intrinsic scatter ( $\delta_i$ ) in [Fe/H] (blue) and in radial gradient of [Fe/H] (red) plotted with  $\sigma$ . The unit associated with [Fe/H] is dex and that with radial gradient is dex/log( $R/R_e$ ).

in gradient. The arguments just articulated for support of a  $\sigma$ -dependent merger likelihood apply in the case of [Fe/H] as well.



**Figure 25.** The intrinsic scatter ( $\delta_i$ ) in abundances of C (blue), N (orange), Na (green), and Mg (red) plotted with  $\sigma$ . The unit is dex for  $\delta_i$ .

Fig. 25 shows the  $\delta_i$  values in C, N, Na, and Mg abundances. The intrinsic scatter in C abundance is the least, with Mg a close second. Apart from the first  $\sigma$  bin, N abundance has nearly constant  $\delta_i$  of 0.1 dex for all the other  $\sigma$  bins. The high value of  $\delta_i$  in N for smaller galaxies ( $\log(\sigma) < 2.0$ ) might shed light on the time-scale of chemical enrichment in them. If N from intermediate-mass stars is important, a variation in N abundance implies a variation in formation timescale. It is plausible that these variations would be attenuated in galaxies with richer merger histories. The  $\delta_i$  for Na abundance is  $\sim 0.14$  dex for the first three  $\sigma$  bins and decreasing marginally to 0.12 dex for the



last two high  $\sigma$  bins. This behavior of Na is not yet fully understood, but additional absorption of Na in the interstellar medium (ISM) could increase inferred [Na/R] in some galaxies and increase scatter.

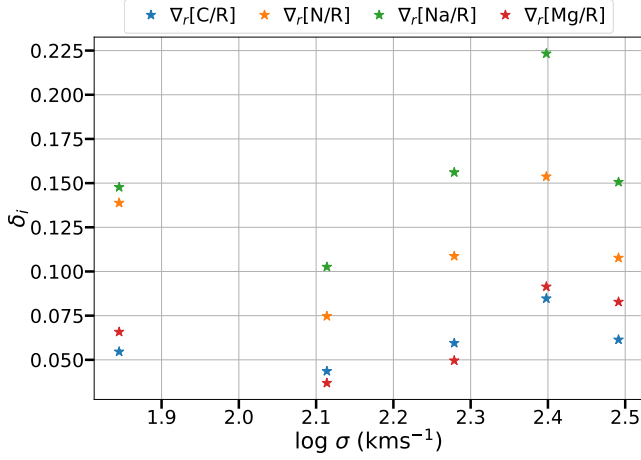


**Figure 26.** The intrinsic scatter ( $\delta_i$ ) in radial gradients for C (blue), N (orange), Na (green), and Mg (red) abundances plotted with  $\sigma$ . The unit is dex/ $\log(R/R_e)$  for  $\delta_i$ .

We show the  $\delta_i$  values in radial gradients of C, N, Na, and Mg abundances in Fig. 26. The most interesting result is the increasing trend of  $\delta_i$  from the second  $\sigma$  bin onwards till the penultimate  $\sigma$  bin, reaching a value of almost a factor of two higher compared to the second  $\sigma$  bin. Surprisingly, the  $\delta_i$  in all the elements for the highest  $\sigma$  bin drops to a lower value. Radial gradients in C and Mg have the lowest values in  $\delta_i$  followed by N and then Na. This similar trend is also seen in Fig. 25. It is noteworthy that radial gradients in Na have significantly higher  $\delta_i$  compared to other elements considered in this work reaching as high as 0.22 dex/ $\log(R/R_e)$  in the fourth  $\sigma$  bin. In conjunction with the Fig. 20, it can be stated that there is a significant and as-yet-unexplained anomaly regarding Na, which has not been sufficiently addressed in the existing body of literature. ISM absorption may play a small role, but the overall coherence of Na with Mg and other elements argues that ISM absorption is the exception rather than the rule.

Table 5 summarises the results for our  $\delta_i$  calculations. The  $\delta_i$  values are rounded to two decimal places in the table.

As is mentioned earlier, there have not been many studies on the topic of intrinsic scatter in stellar population parameters like the age. Gallazzi et al. (2005) showed that their age and [Fe/H] estimates contain significant intrinsic scatter at all masses of galaxies. The authors also note that there is a decreasing trend in the scatter with mass for [Fe/H] and very flat trend for age. In our work, both age and [Fe/H] show a decreasing trend in  $\delta_i$  with  $\sigma$ . The val-

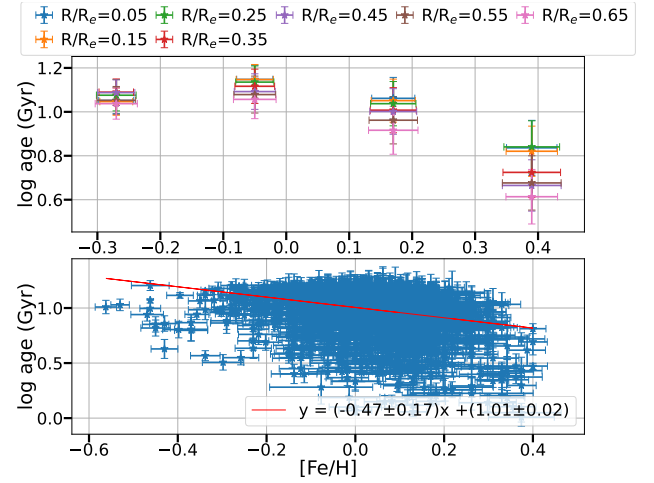


**Figure 27.** The (log of) mean age is plotted against [Fe/H] with errorbars. The top panel shows the mean values for each [Fe/H] bin ([Fe/H] bins are described in Table 3) color coded by annuli. The legend on top shows the middle value for each radial bin. The bottom panel shows the mean age of each galaxy's 3<sup>rd</sup> annulus. The legend describes the best fit line with 'y' as the mean age and 'x' as the [Fe/H].

ues reported by Gallazzi et al. (2005) are close to the  $\delta_i$  values in age and [Fe/H] that we report in this work. Price et al. (2011) also reported a decrease in intrinsic scatter in [Fe/H] with increasing  $\sigma$ .

We now provide brief remarks on the age-[Fe/H] relation. Fig. 27 shows the distribution of age with [Fe/H] for each annulus grouped by [Fe/H] (top panel) and for the 3<sup>rd</sup> annulus of each individual galaxy (bottom panel). The  $\delta_i$  in age and [Fe/H] is sufficient to explain the errorbars in top panel of Fig. 27. We see a decreasing trend of age with [Fe/H] (at least for the last three [Fe/H] bins). The trend-line shows that the age of ETGs decrease by as much as 0.4 dex (equivalent to 2.5 Gyr) for an increase in [Fe/H] by 1 dex. One of the first works on characterizing age-[Fe/H] relation was done by Worthey et al. (1995). They showed that E/S0 galaxies follow the direction of *null spectral change* characterized by  $\Delta \log Z / \Delta \log \text{age} = -2/3$ . The slope of -0.47 dex/dex that we derived in log age - [Fe/H] plane (bottom panel of Fig. 27) is not too far away from the numerical value of -2/3 ( $\approx -0.67$ ). A very similar result was reported by other studies that looked into elliptical galaxies in Fornax cluster (Kuntschner 2000) and Coma cluster (Jørgensen 1999; Poggianti et al. 2001). Gallazzi et al. (2005) analyzed almost 26,000 ETGs from SDSS-DR2 and showed that (their Fig. 12) the age-[Fe/H] relation have an anti-correlation for all of their mass bins. Galaxies in different environments also show the trend from old and metal-poor to young and metal-rich in Coma supercluster (Tiwari et al. 2020).

This observed trend of decreasing metallicity with increasing age is a result of chemical evolution of the galaxies

**Table 5.** Table showing the intrinsic scatter ( $\delta_i$ ) in all of the measured astrophysical parameters and their radial gradients for all the  $\sigma$  bins used in this work. The unit for  $\delta_i$  in astrophysical parameters is dex and that for  $\delta_i$  in their radial gradients is dex/log( $R/R_e$ ).

log $\sigma$ Range (km/s)	$\delta_i$ in age	$\delta_i$ in [Fe/H]	$\delta_i$ in [C/R]	$\delta_i$ in [N/R]	$\delta_i$ in [Na/R]	$\delta_i$ in [Mg/R]	$\delta_i$ in $\nabla_r$ (age)	$\delta_i$ in $\nabla_r$ [Fe/H]	$\delta_i$ in $\nabla_r$ [C/R]	$\delta_i$ in $\nabla_r$ [N/R]	$\delta_i$ in $\nabla_r$ [Na/R]	$\delta_i$ in $\nabla_r$ [Mg/R]
[1.6, 2]	0.20	0.15	0.06	0.15	0.13	0.08	0.10	0.15	0.05	0.14	0.15	0.06
[2, 2.2]	0.18	0.11	0.06	0.12	0.14	0.06	0.12	0.14	0.04	0.07	0.10	0.04
[2.2, 2.34]	0.15	0.09	0.05	0.10	0.13	0.06	0.20	0.14	0.06	0.10	0.15	0.05
[2.34, 2.45]	0.10	0.11	0.07	0.12	0.12	0.07	0.35	0.19	0.08	0.15	0.22	0.09
[2.45, 2.53]	0.07	0.10	0.04	0.09	0.12	0.06	0.45	0.22	0.06	0.10	0.15	0.08

and their star formation history. Perhaps, elliptical galaxy precursors formed most of their stars early in the Universe's history through rapid, intense starbursts (Partridge & Peebles 1967; De Lucia et al. 2006). At that early stage of Universe's history, the relatively metal-poor gas formed metal poor stars. Elliptical galaxies are often the product of major mergers of smaller galaxies (Toomre & Toomre 1972; Taranu et al. 2015). These mergers can trigger intense star formation early in a galaxy's evolution but can also lead to the expulsion of gas through galactic winds, particularly if supernovae and active galactic nuclei (AGN) are involved (Loewenstein & Mathews 1987; Forman et al. 1990). Thus the decrease in metallicity with increasing age in elliptical galaxies might be explained as a result of rapid early star formation, feedback processes that expel metal-rich gas, and the cessation of star formation early in the galaxy's history.

#### 5.4. Comparison with IllustrisTNG

The Next Generation Illustris (IllustrisTNG) project is a series of magnetohydrodynamical cosmological simulations designed to investigate galaxy formation and evolution within the framework of the  $\Lambda$  Cold Dark Matter ( $\Lambda$  - CDM) cosmological model (Marinacci et al. 2018; Naiman et al. 2018; Nelson et al. 2018; Pillepich et al. 2018; Springel et al. 2018). It builds and improves on the scientific insights and achievements of the original Illustris simulation (Vogelsberger et al. 2014b; Genel et al. 2014). Nine individual elements – hydrogen (H), helium (He), carbon (C), nitrogen (N), oxygen (O), neon (Ne), magnesium (Mg), silicon (Si), and iron (Fe) – were explicitly tracked throughout the IllustrisTNG simulation (Naiman et al. 2018). In this work, we compare our results with those of publicly available IllustrisTNG data (Nelson et al. 2019). Only a couple of studies have so far compared the results of the IllustrisTNG simulations with the observations (Naiman et al. 2018; Pulsoni et al. 2020). We sought to eliminate this scarcity as an additional task in this work.

Selection of theoretical data began with selecting 1000 halo IDs from the ‘deep learning morphologies’ list

(Huertas-Company et al. 2019) that were ETGs at a probability of 60% or greater. For computation of half light radii, we assumed the halos had spherical symmetry and iterated to the radius at which half the particles lay inside and half outside. We adopted this radius as  $R_e$  for the computation of stellar particle velocity dispersion and radially-dependent quantities. Mean ages are  $V$ -band weighted averages of the star particle formation ages.

We compare our results with that of IllustrisTNG in two different ways: (1) grouped by  $\sigma$  following the binning scheme outlined in the Table 2 and plotted versus  $R/R_e$ , and (2) ungrouped versus  $\sigma$  using the 3<sup>rd</sup> annulus for the MaNGA galaxies. We provide all the comparison plots in Appendix A.

*Mean age comparison.* Fig. 28 shows the comparison for IllustrisTNG and MaNGA ages. In the left-hand panel of the plot we see that the IllustrisTNG galaxies (solid lines) in all  $\sigma$  bins show a very flat radial trend in age and it is very well matches our calculations (stars with errorbars) of age radial gradients within each  $\sigma$  bin. The right-hand panel shows the age of each individual IllustrisTNG galaxy (in red cross) plotted against their  $\sigma$ , overlaid on our findings (in blue star) for the age at 3<sup>rd</sup> annulus for each MaNGA galaxy. We again see striking similarity between the IllustrisTNG results and our work. Although the scatter in IllustrisTNG measurements is less across all  $\sigma$  values compared to MaNGA, it is interesting to note that scatter decreases with increasing  $\sigma$  for IllustrisTNG simulation as well.

*Mean [Fe/H] comparison.* Two panels in Fig. 29 shows comparison between IllustrisTNG and MaNGA results for [Fe/H]. Except for a zero point shift of about a factor of two (IllustrisTNG being more metal rich), the morphologies of the trends are remarkably similar. The spatial gradients are quantitatively similar, and even show the steepening with increasing  $\sigma$  (left-hand panel). IllustrisTNG results also show a decreasing trend in [Fe/H] for galaxies with  $\log(\sigma) > 2.0$  (right-hand panel). Our MaNGA sample might place the inflection point at  $\log(\sigma) > 2.1$ , instead, but the existence of the inflection is a remarkable success for IllustrisTNG. Because COMPFIT will not return values of [Fe/H]

higher than 0.4, we cannot comment on the small number of IllustrisTNG galaxies that scatter to higher  $[\text{Fe}/\text{H}]$  values. We also observe a  $\sim 1\%$  fraction of galaxies that scatter to low abundance. These are not reflected the theoretical simulation.

*Mean  $[\text{X}/\text{Fe}]$  comparison.* While considering the individual elements (Fig. 30 for C, Fig. 31 for N, and Fig. 32 for Mg), the most striking aspect is the zeropoint offsets. To reiterate our methods, we include magnesium amplification for the first time, so our abundance results should approach actual  $[\text{X}/\text{Fe}]$  values for the first time in the literature. IllustrisTNG, on the other hand, will have adjusted their assumptions of stellar element yields to follow earlier estimates. Therefore, these zeropoint offsets should be no surprise. Parenthetically, Naiman et al. (2018) also reported an overabundance of magnesium for Milky Way-like galaxies in the IllustrisTNG simulation. Looking past that, the shapes of the data clouds are qualitatively similar. The abundance inflection at  $\log(\sigma) = 2$  is seen in all elements in both theory and observation.

*The inflection at  $\log(\sigma) \approx 2$ .* The fact that IllustrisTNG simulations qualitatively reproduce the chemical “phase change” at  $\log(\sigma) \approx 2$  is a success of the theory. To our knowledge, no author has pointed out this particular success before. Low- $\sigma$  galaxies are effective at Fe enrichment, but high- $\sigma$  galaxies favor light metal enrichment to such a degree that  $[\text{Fe}/\text{H}]$  falls with increasing  $\sigma$ . By itself, this implies that high- $\sigma$  galaxies cannot simply be dry mergers of  $\sim 100 \text{ km s}^{-1}$  subunits: the inherited abundance pattern does not persist. It is also hard to imagine a monolithic collapse scenario in which galaxies with shallower potential wells retain *more* iron, since supernova winds should be relatively more effective in low- $\sigma$  galaxies. But IllustrisTNG demonstrates that the hierarchical merger picture can thread the needle between extremes and reproduce the age- $\sigma$  trend along with the chemical inflection at  $\log(\sigma) \approx 2$ .

*Nitrogen.* The large scatter in N, especially compared to IllustrisTNG, is remarkable. Because the scatter in  $[\text{N}/\text{Fe}]$  is astrophysical, it is clear that much information is being carried in this tracer element regarding the chemical histories of galaxies. Nitrogen of some quantity is produced instantly in supernovae, at young ages in WR stars and other massive stars, at intermediate ages via CNO processed material, and even in old red giants by mass loss after first dredge-up. Due to the unsolved status of mass loss in stars, the balancing of yields from these sources is not predictable from first principles. However, our results here hint at the importance of CNO processed material. Since increased N comes at the expense of C in the CNO cycle, one might expect an anticorrelation between the two abundances, other things being equal. In fact, we nearly

observe this because the correlation between  $[\text{N}/\text{R}]$  and  $[\text{C}/\text{R}]$  gradients is the weakest. In the annulus 3 plots,  $[\text{N}/\text{R}]$  correlates least tightly with  $[\text{C}/\text{R}]$  and  $[\text{Na}/\text{R}]$ . The possibility that we see the effects of CNO processing in these data is real.

*ADF comparison.* We compared the Abundance Distribution Function (ADF) used in this study with six halos taken from IllustrisTNG, as shown in Fig. 33. The analytical ADF formula was taken from Worthey et al. (2005) and Tang et al. (2014), and we used the ‘normal’ width ADF to derive peak  $[\text{Fe}/\text{H}]$  from MaNGA galaxies. The ‘normal’ ADF has FWHM width of 0.65 dex. The six IllustrisTNG ADFs average to FWHM = 0.67 dex, and the overall shapes are similar. This shows the consistency between our assumptions, which are based on observations in the local universe, and the IllustrisTNG calculations. Our composite models should be free of bias as compared to IllustrisTNG, at least along the dimension of abundance-compositeness. On the other hand, the overall chemical evolution assumptions in IllustrisTNG give ADFs that resemble observations, except for a small parcel of relic stars at very low metallicity (Population III stars, not illustrated in Fig. 33) that are so far unseen in the local universe, and therefore may not exist.

## 6. CONCLUSION

In this work we have used the Worthey (1994) stellar population models to investigate stellar population age and abundance parameters and their radial gradients for 2417 SDSS MaNGA ETGs. The models are composite in metallicity with an ADF that resembles nearby galaxies. They also include an improvement, magnesium amplification, that allows them to approach true  $[\text{X}/\text{H}]$  and  $[\text{X}/\text{R}]$  values for the first time. Thus, these results supersede previous results by models without abundance-sensitive isochrone shifts, which, as of this writing, is all past work. That said, the improved results are not dramatically different, albeit with interesting new behavior in N and Na. The models are inverted to infer mean age, ADF peak  $[\text{Fe}/\text{H}]$ , and mean elemental abundances for C, N, Na, and Mg for each elliptical annulus within each of the 2417 galaxies. We investigate primarily trends with  $\sigma$  and  $[\text{Fe}/\text{H}]$  in this paper.

We find positive correlation between the age and size of the galaxies implying more massive ETGs have older age. But for  $[\text{Fe}/\text{H}]$ , this trend reverses such that galaxies starting at  $\log\sigma \approx 2$  trend toward lower  $[\text{Fe}/\text{H}]$ , while galaxies at all  $\sigma$  trend toward higher C, N, Na, and Mg with increased  $\sigma$ . The light element abundances strengthen faster than  $[\text{Fe}/\text{H}]$  falls, so the most massive galaxies are enriched in heavy elements ( $Z$ ) overall. These two findings can be merged together to conclude that older galaxies have lower  $[\text{Fe}/\text{H}]$  but higher light metals and  $Z$ . The light metals show

a negative correlation with  $[\text{Fe}/\text{H}]$ , presumably implying a spread of Type Ia/Type II supernova yield contributions.

Among 7 annuli within each galaxy, a nearly flat average radial gradient in age is accompanied by large individual galaxy scatter. That is, nearly as many galaxies show a younger center as show a younger portion at  $0.65 R_e$ . Gradients in abundances are negative but nearly flat for low- $\sigma$  galaxies. For high- $\sigma$  galaxies, the gradients are more strongly negative, with the most emphatic gradients in Fe and Na.

In terms of galaxy formation and evolution, our findings are more consistent with formation of ETGs via *merging* (citations in §1) rather than strong *monolithic collapse* (citations in §1). Davies et al. (1993) proposes a scenario where smaller galactic subunits are formed by dissipational collapse which underwent dissipationless major mergers in subsequent times. This theory is supported in other works on stellar population parameter gradients (Kobayashi 2004; Goddard et al. 2017). In our work, the strong dependence of  $[\text{Fe}/\text{H}]$  radial gradient values on  $\sigma$  poses a problem to such theory. A merging dominant galactic evolution pathway is more apt in explaining our results. The radial gradients in C, N, and Mg also correspond well with the negative radial gradient in  $[\text{Fe}/\text{H}]$  pointing to the fact that overall element enrichment ( $Z$ ) varies with galactocentric radius, with metal-rich centers and relatively metal-poor outer parts (Mehlert et al. 2003). While some cosmological simulations of galaxy formation support a two-phase formation model (Oser et al. 2010), our findings suggest that merger events were the primary drivers of galaxy evolution, with a minor contribution from dissipational collapse.

We also discussed the observed trend of having more metal poor population in older elliptical galaxies and more metal rich stars in the younger ellipticals. This result agrees well with a number of previous studies and points to continued chemical enrichment in a substantial number of ETGs across much of cosmic time.

The internal scatter ( $\delta_i$ ) calculated in this work is an inference only rarely exploited in the literature. We found a decreasing trend for  $\delta_i$  in both the age and  $[\text{Fe}/\text{H}]$  with the  $\sigma$ . The  $\delta_i$  in radial gradients in those two quantities are sufficient to explain the scatter in the radial gradients calculated for them. The  $\delta_i$  in elemental abundances and their gradients show in general lower  $\delta_i$  values compared to the age and  $[\text{Fe}/\text{H}]$ . The only exception being Na. It is worth investing in the future the stand alone behaviour of

Na compared to other elements considered in this work. As a note for future work, we also intend to study the effect of environment on the intrinsic scatter of astrophysical parameters.

Aside from substantial zero point and scale shifts in the abundances, we found a remarkable similarity between our work and the IllustrisTNG simulation in the abundance- $\sigma$  slope inflection that occurs at  $\log \sigma \approx 2$ . The IllustrisTNG simulation result of  $[\text{Fe}/\text{H}]$  decreasing (for  $\log(\sigma) > 2.0$ ) with  $\sigma$  matches very well with our work. Also, the light elements (C, N, and Mg) show a prominent increased abundance for  $\log(\sigma) > 2.0$  both in IllustrisTNG and our work. This potentially points to better and more efficient chemical enrichment in light elements in the subunits that eventually merge to form the largest ETGs.

#### ACKNOWLEDGEMENTS

Funding for the Sloan Digital Sky Survey IV has been provided by the Alfred P. Sloan Foundation, the U.S. Department of Energy Office of Science, and the Participating Institutions.

SDSS-IV acknowledges support and resources from the Center for High Performance Computing at the University of Utah. The SDSS website is [www.sdss4.org](http://www.sdss4.org).

SDSS-IV is managed by the Astrophysical Research Consortium for the Participating Institutions of the SDSS Collaboration including the Brazilian Participation Group, the Carnegie Institution for Science, Carnegie Mellon University, Center for Astrophysics | Harvard & Smithsonian, the Chilean Participation Group, the French Participation Group, Instituto de Astrofísica de Canarias, The Johns Hopkins University, Kavli Institute for the Physics and Mathematics of the Universe (IPMU) / University of Tokyo, the Korean Participation Group, Lawrence Berkeley National Laboratory, Leibniz Institut für Astrophysik Potsdam (AIP), Max-Planck-Institut für Astronomie (MPIA Heidelberg), Max-Planck-Institut für Astrophysik (MPA Garching), Max-Planck-Institut für Extraterrestrische Physik (MPE), National Astronomical Observatories of China, New Mexico State University, New York University, University of Notre Dame, Observatório Nacional / MCTI, The Ohio State University, Pennsylvania State University, Shanghai Astronomical Observatory, United Kingdom Participation Group, Universidad Nacional Autónoma de México, University of Arizona, University of Colorado Boulder, University of Oxford, University of Portsmouth, University of Utah, University of Virginia, University of Washington, University of Wisconsin, Vanderbilt University, and Yale University.

#### APPENDIX



## A. PLOTS SHOWING COMPARISON WITH ILLUSTRIS

This section of the appendix contains figures 28, 29, 30, 31, 32, and 33 elucidating comparison between our results and IllustrisTNG results for age, [Fe/H], [C/R], [N/R], [Mg/R], and ADF respectively.

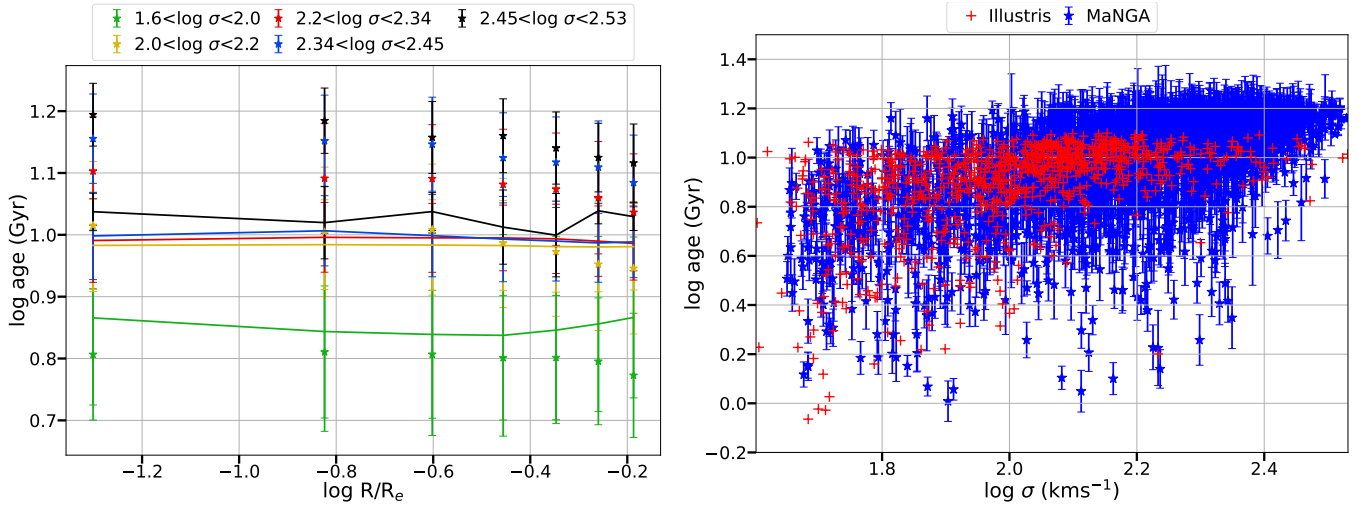


**Figure 28.** The left panel shows how the mean age for different  $\sigma$  bins are changing with distance from the center of the galaxy. The solid lines show results from the Illustris and the stars with errorbars show results from our work. Both the lines and symbols use same color codes for different  $\sigma$  bins. The right panel shows how the age of each individual Illustris galaxy (in red plus) and age from 3<sup>rd</sup> annulus of each MaNGA galaxy (in blue star) are changing with  $\sigma$ . MaNGA galaxies have errors associated with each data point.

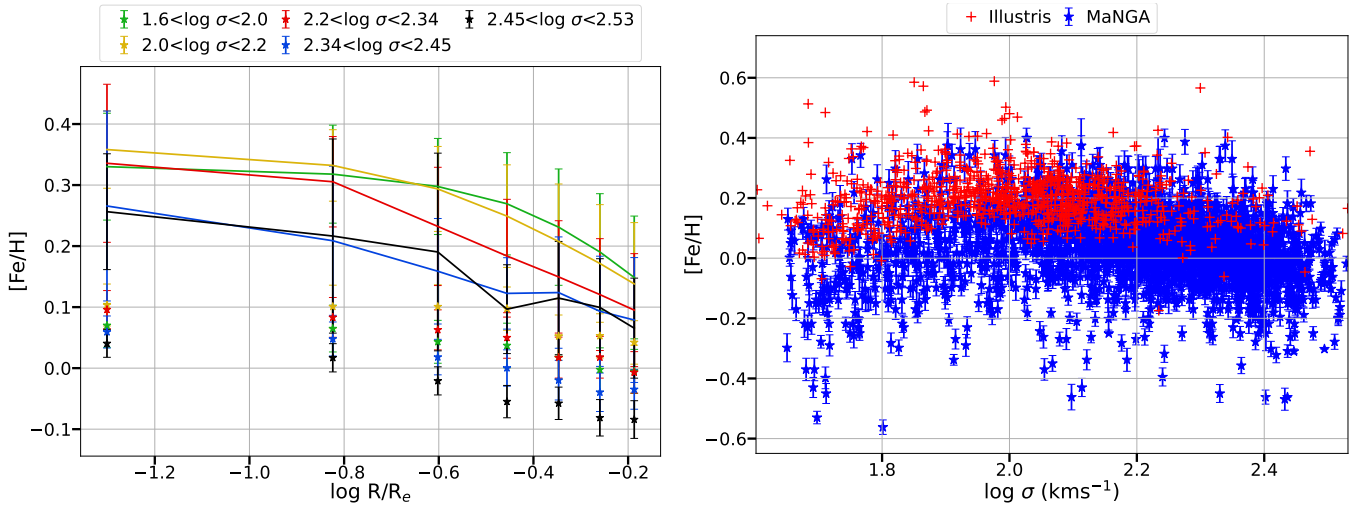


**Figure 29.** The left panel shows how the mean [Fe/H] for different  $\sigma$  bins are changing with distance from the center of the galaxy. The solid lines show results from the Illustris and the stars with errorbars show results from our work. Both the lines and symbols use same color codes for different  $\sigma$  bins. The right panel shows how the [Fe/H] of each individual Illustris galaxy (in red plus) and age from 3<sup>rd</sup> annulus of each MaNGA galaxy (in blue star) are changing with  $\sigma$ . MaNGA galaxies have errors associated with each data point.

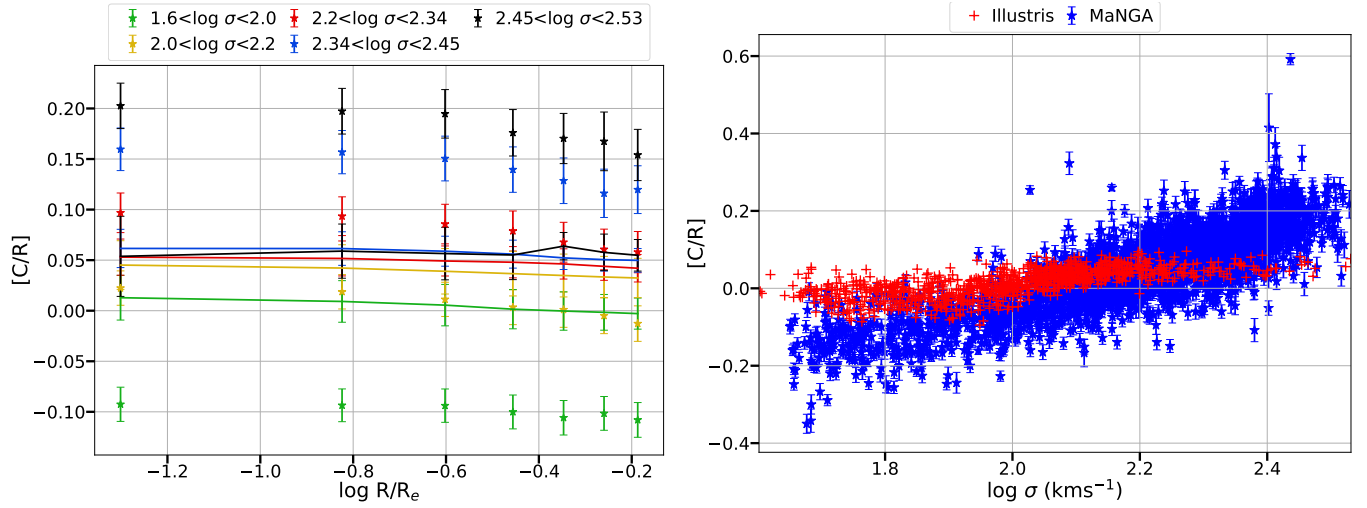


**Figure 30.** The left panel shows how the mean carbon abundance for different  $\sigma$  bins are changing with distance from the center of the galaxy. The solid lines show results from the Illustris and the stars with errorbars show results from our work. Both the lines and symbols use same color codes for different  $\sigma$  bins. The right panel shows how the  $[C/R]$  of each individual Illustris galaxy (in red plus) and age from  $3^{\text{rd}}$  annulus of each MaNGA galaxy (in blue star) are changing with  $\sigma$ . MaNGA galaxies have errors associated with each data point.

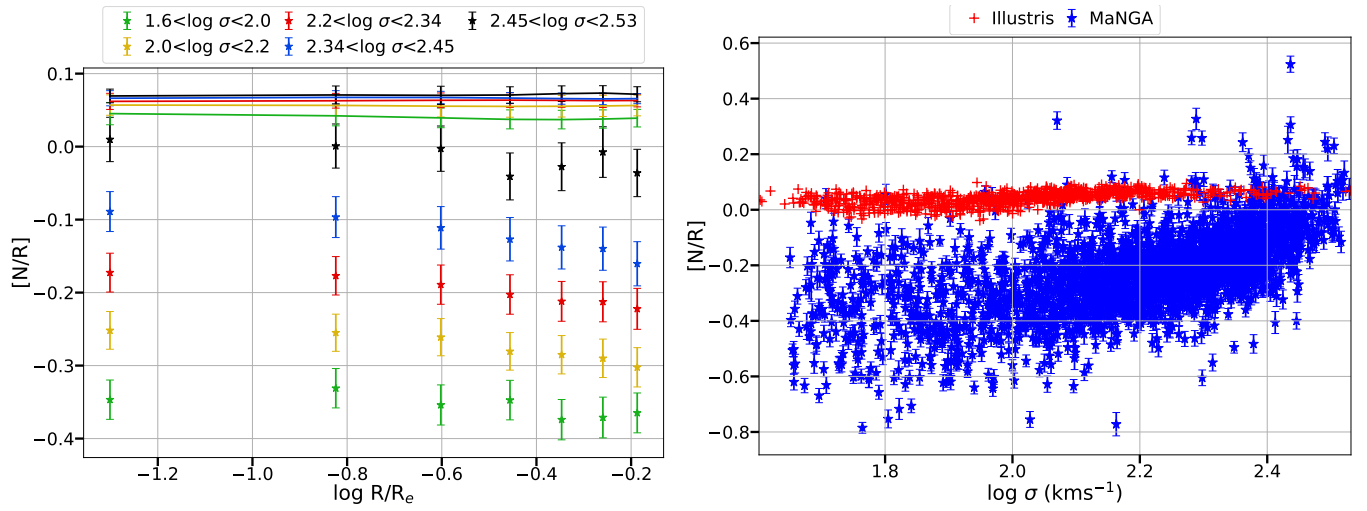


**Figure 31.** The left panel shows how the mean nitrogen abundance for different  $\sigma$  bins are changing with distance from the center of the galaxy. The solid lines show results from the Illustris and the stars with errorbars show results from our work. Both the lines and symbols use same color codes for different  $\sigma$  bins. The right panel shows how the  $[N/R]$  of each individual Illustris galaxy (in red plus) and age from  $3^{\text{rd}}$  annulus of each MaNGA galaxy (in blue star) are changing with  $\sigma$ . MaNGA galaxies have errors associated with each data point.

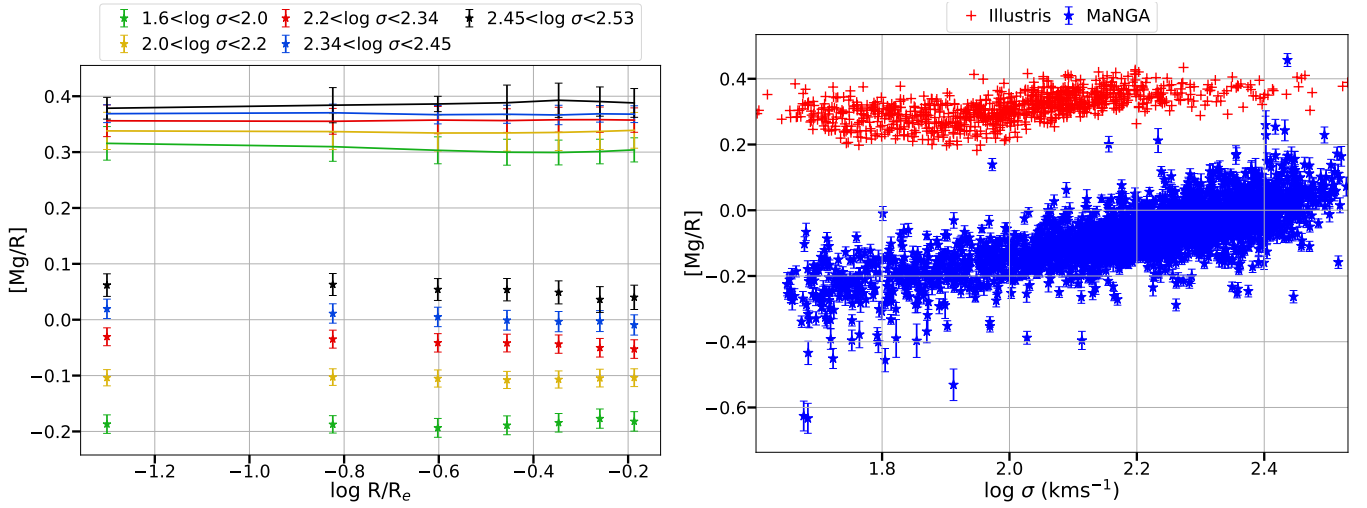


**Figure 32.** The left panel shows how the mean magnesium abundance for different  $\sigma$  bins are changing with distance from the center of the galaxy. The solid lines show results from the Illustris and the stars with errorbars show results from our work. Both the lines and symbols use same color codes for different  $\sigma$  bins. The right panel shows how the  $[Mg/R]$  of each individual Illustris galaxy (in red plus) and age from  $3^{rd}$  annulus of each MaNGA galaxy (in blue star) are changing with  $\sigma$ . MaNGA galaxies have errors associated with each data point.

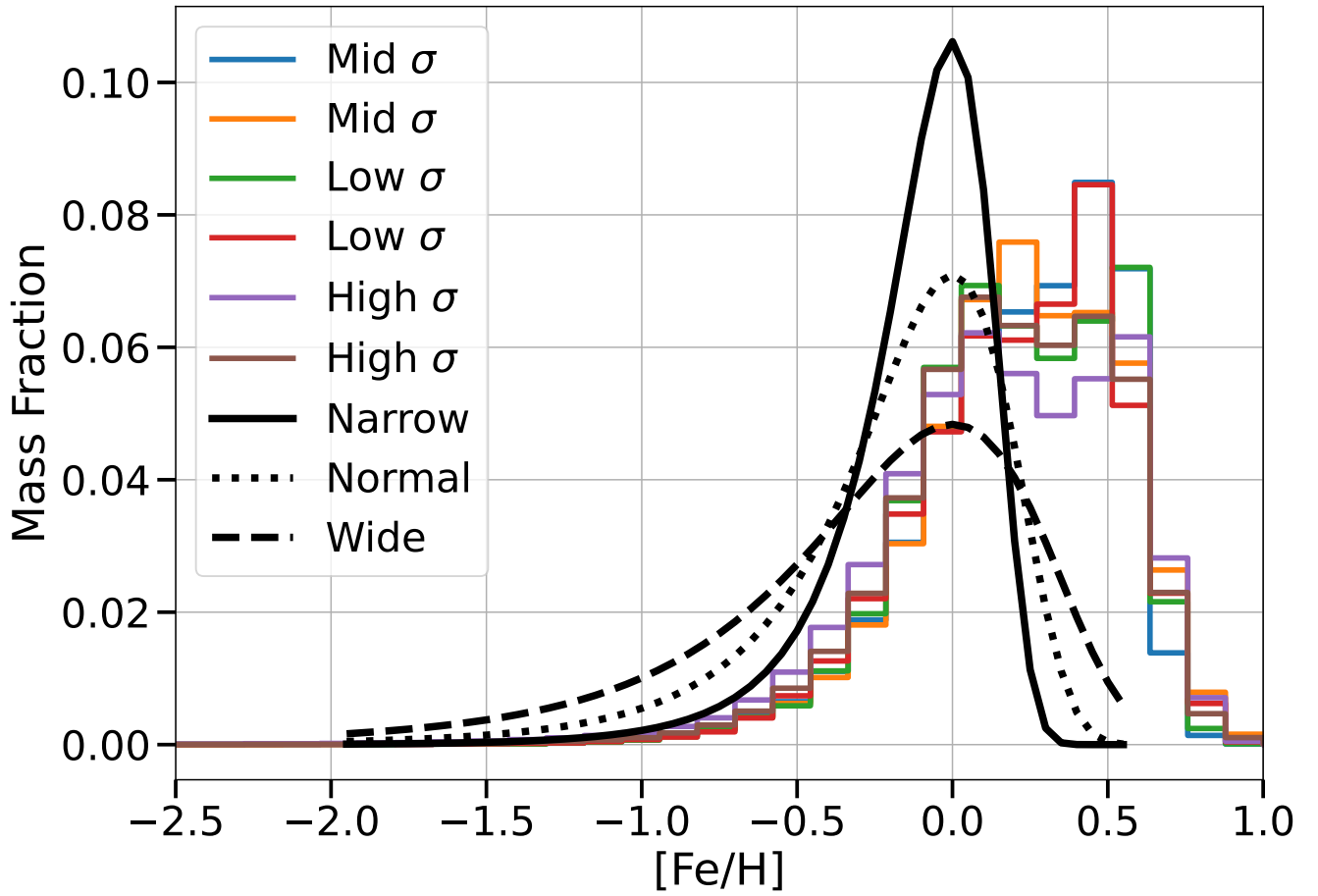


**Figure 33.** The Abundance Distribution Function (ADF) for individual Illustris galaxies (in colored solid lines) plotted alongwith ADF used in this work (black lines with different styles). In this work, we have specifically used the 'Normal' ADF which resembles well with the Illustris ADF.

## B. SPECTRAL FEATURE TABLE

This section of the appendix contains a part of the table showing the details of the spectral features used in conjunction with the [Worthey \(1994\)](#) model to calculate age, [Fe/H], and elemental abundances. The full table is available online at [\[link to be inserted\]](#).

**Table 6.** List of all the spectral features used in the COMPFIT program (full table is available online at [\[link to be inserted\]](#)). The acronyms are as follows: IB=Index Band, BC=Blue Continuum, RC=Red Continuum. The “Start” and “End” phrases are used to denote the start and end wavelengths of the passbands in Å. The “Unit” column specifies if the index used is an atomic feature (denoted by 0; units: Å) or a molecular feature (denoted by 1; units: mag).

Feature Name	IB Start	IB End	BC Start	BC End	RC Start	RC End	Unit
CN <sub>1</sub>	4142.125	4177.125	4080.125	4117.625	4284.125	4244.125	1
CN <sub>2</sub>	4142.125	4177.125	4083.875	4096.375	4284.125	4244.125	1
Ca4227	4222.25	4234.75	4211	4219.75	4251	4241	0

## C. MONTE CARLO (MC) RESULTS

This section of the appendix shows a part of the table with the results from our MC simulation. The full table is available at [\[link to be inserted\]](#).

**Table 7.** Table showing the values of our derived astrophysical parameters, their radial gradients, and corresponding errors. This is a part of the table and the full table is available online at [\[link to be inserted\]](#).

Name	R/R <sub>e</sub>	$\sigma_{cen}$ ( $km s^{-1}$ )	$\sigma_{ann}$ ( $km s^{-1}$ )	log age	Error in log age	$\nabla_r$ log age	Error in $\nabla_r$ log age	[Fe/H]	Error in [Fe/H]	$\nabla_r$ [Fe/H]	Error in $\nabla_r$ [Fe/H]	[C/R]	Error in [C/R]
11867-3703_ann_0	0.05	157.37	186.35	1.043	0.124	0.027	0.4	0.138	0.042	-0.006	0.14	0.044	0.023
11867-3703_ann_2	0.25	157.37	166.36	1.078	0.103	0.027	0.4	0.102	0.037	-0.006	0.14	0.062	0.02
11867-3703_ann_3	0.35	157.37	162.46	1.099	0.106	0.027	0.4	0.098	0.035	-0.006	0.14	0.047	0.018
11867-3703_ann_4	0.45	157.37	159.61	1.104	0.074	0.027	0.4	0.102	0.028	-0.006	0.14	0.045	0.018
11867-3703_ann_5	0.55	157.37	157.37	1.076	0.111	0.027	0.4	0.098	0.036	-0.006	0.14	0.045	0.017
11867-3703_ann_6	0.65	157.37	155.53	1.152	0.088	0.027	0.4	0.05	0.032	-0.006	0.14	0.047	0.015
11743-1902_ann_0	0.05	212.06	251.12	1.045	0.084	-0.029	0.09	0.05	0.027	-0.05	0.03	0.078	0.015
11743-1902_ann_1	0.15	212.06	232.41	1.031	0.097	-0.029	0.09	0.05	0.035	-0.05	0.03	0.079	0.02
11743-1902_ann_2	0.25	212.06	224.18	1.024	0.085	-0.029	0.09	0.03	0.027	-0.05	0.03	0.077	0.019
11743-1902_ann_3	0.35	212.06	218.93	1.012	0.094	-0.029	0.09	0.018	0.028	-0.05	0.03	0.078	0.019
11743-1902_ann_4	0.45	212.06	215.08	1.025	0.093	-0.029	0.09	0.018	0.032	-0.05	0.03	0.074	0.02
11743-1902_ann_5	0.55	212.06	212.06	1.012	0.083	-0.029	0.09	0.005	0.029	-0.05	0.03	0.076	0.018

$\nabla_r$ [C/R]	Error in $\nabla_r$ [C/R]	[N/R]	Error in [N/R]	$\nabla_r$ [N/R]	Error in $\nabla_r$ [N/R]	[Na/R]	Error in [Na/R]	$\nabla_r$ [Na/R]	Error in $\nabla_r$ [Na/R]	[Mg/R]	Error in [Mg/R]	$\nabla_r$ [Mg/R]	Error in $\nabla_r$ [Mg/R]
0.002	0.023	-0.309	0.023	-0.026	0.026	-0.169	0.023	-0.008	0.025	-0.147	0.012	0.008	0.014
0.002	0.023	-0.333	0.026	-0.026	0.026	-0.163	0.023	-0.008	0.025	-0.161	0.012	0.008	0.014
0.002	0.023	-0.307	0.031	-0.026	0.026	-0.165	0.027	-0.008	0.025	-0.122	0.015	0.008	0.014
0.002	0.023	-0.348	0.021	-0.026	0.026	-0.173	0.027	-0.008	0.025	-0.157	0.012	0.008	0.014
0.002	0.023	-0.341	0.028	-0.026	0.026	-0.181	0.024	-0.008	0.025	-0.135	0.016	0.008	0.014
0.002	0.023	-0.329	0.025	-0.026	0.026	-0.177	0.024	-0.008	0.025	-0.135	0.013	0.008	0.014
-0.001	0.02	-0.151	0.03	-0.002	0.037	0.031	0.029	0.077	0.031	-0.033	0.016	-0.002	0.017
-0.001	0.02	-0.149	0.028	-0.002	0.037	0.039	0.031	0.077	0.031	-0.035	0.017	-0.002	0.017
-0.001	0.02	-0.142	0.031	-0.002	0.037	0.07	0.037	0.077	0.031	-0.042	0.019	-0.002	0.017
-0.001	0.02	-0.158	0.026	-0.002	0.037	0.086	0.027	0.077	0.031	-0.044	0.017	-0.002	0.017
-0.001	0.02	-0.172	0.025	-0.002	0.037	0.071	0.033	0.077	0.031	-0.038	0.017	-0.002	0.017
-0.001	0.02	-0.15	0.031	-0.002	0.037	0.128	0.028	0.077	0.031	-0.028	0.016	-0.002	0.017

NOTE— $\sigma_{cen}$  is the  $\sigma$  at the position of the 5<sup>th</sup> annulus from the center of the galaxy and  $\sigma_{ann}$  is the individual  $\sigma$  for each annulus.

## REFERENCES

- Abdurro'uf, Accetta, K., Aerts, C., et al. 2022, *ApJS*, 259, 35, doi: [10.3847/1538-4365/ac4414](https://doi.org/10.3847/1538-4365/ac4414)
- Alibés, A., Labay, J., & Canal, R. 2001, *A&A*, 370, 1103, doi: [10.1051/0004-6361:20010296](https://doi.org/10.1051/0004-6361:20010296)
- Alton, P. D., Smith, R. J., & Lucey, J. R. 2018, *MNRAS*, 478, 4464, doi: [10.1093/mnras/sty1242](https://doi.org/10.1093/mnras/sty1242)
- Bacon, R., Copin, Y., Monnet, G., et al. 2001, *MNRAS*, 326, 23, doi: [10.1046/j.1365-8711.2001.04612.x](https://doi.org/10.1046/j.1365-8711.2001.04612.x)
- Bekki, K., & Shioya, Y. 1999, *ApJ*, 513, 108, doi: [10.1086/306833](https://doi.org/10.1086/306833)
- Belfiore, F., Westfall, K. B., Schaefer, A., et al. 2019, *AJ*, 158, 160, doi: [10.3847/1538-3881/ab3e4e](https://doi.org/10.3847/1538-3881/ab3e4e)
- Bender, R., Burstein, D., & Faber, S. M. 1992, *ApJ*, 399, 462, doi: [10.1086/171940](https://doi.org/10.1086/171940)
- Bender, R., & Surma, P. 1992, *A&A*, 258, 250
- Berg, D. A., Erb, D. K., Henry, R. B. C., Skillman, E. D., & McQuinn, K. B. W. 2019, *ApJ*, 874, 93, doi: [10.3847/1538-4357/ab020a](https://doi.org/10.3847/1538-4357/ab020a)
- Blakeslee, J. P., Jordán, A., Mei, S., et al. 2009, *ApJ*, 694, 556, doi: [10.1088/0004-637X/694/1/556](https://doi.org/10.1088/0004-637X/694/1/556)
- Blanton, M. R., Bershady, M. A., Abolfathi, B., et al. 2017, *AJ*, 154, 28, doi: [10.3847/1538-3881/aa7567](https://doi.org/10.3847/1538-3881/aa7567)
- Bruzual, G., & Charlot, S. 2003, *MNRAS*, 344, 1000, doi: [10.1046/j.1365-8711.2003.06897.x](https://doi.org/10.1046/j.1365-8711.2003.06897.x)
- Bundy, K., Bershady, M. A., Law, D. R., et al. 2015, *ApJ*, 798, 7, doi: [10.1088/0004-637X/798/1/7](https://doi.org/10.1088/0004-637X/798/1/7)
- Cappellari, M. 2017, *MNRAS*, 466, 798, doi: [10.1093/mnras/stw3020](https://doi.org/10.1093/mnras/stw3020)
- Cappellari, M., & Copin, Y. 2003, *MNRAS*, 342, 345, doi: [10.1046/j.1365-8711.2003.06541.x](https://doi.org/10.1046/j.1365-8711.2003.06541.x)
- Cappellari, M., Emsellem, E., Krajnović, D., et al. 2011, *MNRAS*, 413, 813, doi: [10.1111/j.1365-2966.2010.18174.x](https://doi.org/10.1111/j.1365-2966.2010.18174.x)
- Carlberg, R. G., & Freedman, W. L. 1985, *ApJ*, 298, 486, doi: [10.1086/163634](https://doi.org/10.1086/163634)
- Carollo, C. M., Danziger, I. J., & Buson, L. 1993, *MNRAS*, 265, 553, doi: [10.1093/mnras/265.3.553](https://doi.org/10.1093/mnras/265.3.553)
- Chiappini, C., Matteucci, F., & Gratton, R. 1997, *ApJ*, 477, 765, doi: [10.1086/303726](https://doi.org/10.1086/303726)
- Chiappini, C., Romano, D., & Matteucci, F. 2003, *MNRAS*, 339, 63, doi: [10.1046/j.1365-8711.2003.06154.x](https://doi.org/10.1046/j.1365-8711.2003.06154.x)
- Chisholm, J., Tremonti, C. A., Leitherer, C., & Chen, Y. 2017, *MNRAS*, 469, 4831, doi: [10.1093/mnras/stx1164](https://doi.org/10.1093/mnras/stx1164)
- Cicone, C., Maiolino, R., & Marconi, A. 2016, *A&A*, 588, A41, doi: [10.1051/0004-6361/201424514](https://doi.org/10.1051/0004-6361/201424514)
- Cohen, J. G., Blakeslee, J. P., & Ryzhov, A. 1998, *ApJ*, 496, 808, doi: [10.1086/305429](https://doi.org/10.1086/305429)
- Conroy, C. 2013, *ARA&A*, 51, 393, doi: [10.1146/annurev-astro-082812-141017](https://doi.org/10.1146/annurev-astro-082812-141017)
- Conroy, C., Graves, G. J., & van Dokkum, P. G. 2014, *ApJ*, 780, 33, doi: [10.1088/0004-637X/780/1/33](https://doi.org/10.1088/0004-637X/780/1/33)
- Conroy, C., Gunn, J. E., & White, M. 2009, *ApJ*, 699, 486, doi: [10.1088/0004-637X/699/1/486](https://doi.org/10.1088/0004-637X/699/1/486)
- Conroy, C., & van Dokkum, P. G. 2012, *ApJ*, 760, 71, doi: [10.1088/0004-637X/760/1/71](https://doi.org/10.1088/0004-637X/760/1/71)
- Conroy, C., Villaume, A., van Dokkum, P. G., & Lind, K. 2018, *ApJ*, 854, 139, doi: [10.3847/1538-4357/aaab49](https://doi.org/10.3847/1538-4357/aaab49)
- Croom, S. M., Lawrence, J. S., Bland-Hawthorn, J., et al. 2012, *MNRAS*, 421, 872, doi: [10.1111/j.1365-2966.2011.20365.x](https://doi.org/10.1111/j.1365-2966.2011.20365.x)
- Davé, R. 2008, *MNRAS*, 385, 147, doi: [10.1111/j.1365-2966.2008.12866.x](https://doi.org/10.1111/j.1365-2966.2008.12866.x)
- Davé, R., Finlator, K., & Oppenheimer, B. D. 2011, *MNRAS*, 416, 1354, doi: [10.1111/j.1365-2966.2011.19132.x](https://doi.org/10.1111/j.1365-2966.2011.19132.x)
- Davies, R. L., Sadler, E. M., & Peletier, R. F. 1993, *MNRAS*, 262, 650, doi: [10.1093/mnras/262.3.650](https://doi.org/10.1093/mnras/262.3.650)
- De Lucia, G., & Blaizot, J. 2007, *MNRAS*, 375, 2, doi: [10.1111/j.1365-2966.2006.11287.x](https://doi.org/10.1111/j.1365-2966.2006.11287.x)
- De Lucia, G., Springel, V., White, S. D. M., Croton, D., & Kauffmann, G. 2006, *MNRAS*, 366, 499, doi: [10.1111/j.1365-2966.2005.09879.x](https://doi.org/10.1111/j.1365-2966.2005.09879.x)
- De Rossi, M. E., Theuns, T., Font, A. S., & McCarthy, I. G. 2015, *Boletín de la Asociación Argentina de Astronomía La Plata Argentina*, 57, 49
- Dekel, A., & Silk, J. 1986, *ApJ*, 303, 39, doi: [10.1086/164050](https://doi.org/10.1086/164050)
- D'Eugenio, F., Colless, M., van der Wel, A., et al. 2024, *MNRAS*, 532, 1775, doi: [10.1093/mnras/stae1582](https://doi.org/10.1093/mnras/stae1582)
- Di Matteo, P., Pipino, A., Lehnert, M. D., Combes, F., & Semelin, B. 2009, *A&A*, 499, 427, doi: [10.1051/0004-6361/200911715](https://doi.org/10.1051/0004-6361/200911715)
- Drory, N., MacDonald, N., Bershady, M. A., et al. 2015, *AJ*, 149, 77, doi: [10.1088/0004-6256/149/2/77](https://doi.org/10.1088/0004-6256/149/2/77)
- Emsellem, E., Cappellari, M., Peletier, R. F., et al. 2004, *MNRAS*, 352, 721, doi: [10.1111/j.1365-2966.2004.07948.x](https://doi.org/10.1111/j.1365-2966.2004.07948.x)
- Esteban, C., Bresolin, F., García-Rojas, J., & Toribio San Cipriano, L. 2020, *MNRAS*, 491, 2137, doi: [10.1093/mnras/stz3134](https://doi.org/10.1093/mnras/stz3134)
- Faber, S. M., Willmer, C. N. A., Wolf, C., et al. 2007, *ApJ*, 665, 265, doi: [10.1086/519294](https://doi.org/10.1086/519294)
- Falcón-Barroso, J., van de Ven, G., Peletier, R. F., et al. 2011, *MNRAS*, 417, 1787, doi: [10.1111/j.1365-2966.2011.19372.x](https://doi.org/10.1111/j.1365-2966.2011.19372.x)
- Feldmeier-Krause, A., Lonoce, I., & Freedman, W. L. 2021, *ApJ*, 923, 65, doi: [10.3847/1538-4357/ac281e](https://doi.org/10.3847/1538-4357/ac281e)
- Ferreras, I., Scott, N., La Barbera, F., et al. 2019, *MNRAS*, 489, 608, doi: [10.1093/mnras/stz2095](https://doi.org/10.1093/mnras/stz2095)
- Finlator, K., & Davé, R. 2008, *MNRAS*, 385, 2181, doi: [10.1111/j.1365-2966.2008.12991.x](https://doi.org/10.1111/j.1365-2966.2008.12991.x)
- Forbes, D. A., Ponman, T. J., & Brown, R. J. N. 1998, *ApJL*, 508, L43, doi: [10.1086/311715](https://doi.org/10.1086/311715)
- Forbes, D. A., Sánchez-Blázquez, P., & Proctor, R. 2005, *MNRAS*, 361, L6, doi: [10.1111/j.1745-3933.2005.00052.x](https://doi.org/10.1111/j.1745-3933.2005.00052.x)



- Forman, W., Jones, C., Tucker, W., & David, L. P. 1990, in NASA Conference Publication, Vol. 3084, NASA Conference Publication, ed. D. J. Hollenbach & J. Thronson, Harley A., 185
- Franx, M., & Illingworth, G. 1990, *ApJL*, 359, L41, doi: [10.1086/185791](https://doi.org/10.1086/185791)
- Gallazzi, A., Charlot, S., Brinchmann, J., White, S. D. M., & Tremonti, C. A. 2005, *MNRAS*, 362, 41, doi: [10.1111/j.1365-2966.2005.09321.x](https://doi.org/10.1111/j.1365-2966.2005.09321.x)
- Gargiulo, A., Haines, C. P., Merluzzi, P., et al. 2009, *MNRAS*, 397, 75, doi: [10.1111/j.1365-2966.2009.14801.x](https://doi.org/10.1111/j.1365-2966.2009.14801.x)
- Garnett, D. R. 2004, in *Cosmochemistry. The melting pot of the elements*, ed. C. Esteban, R. García López, A. Herrero, & F. Sánchez, 171–216
- Genel, S., Vogelsberger, M., Springel, V., et al. 2014, *MNRAS*, 445, 175, doi: [10.1093/mnras/stu1654](https://doi.org/10.1093/mnras/stu1654)
- Goddard, D., Thomas, D., Maraston, C., et al. 2017, *MNRAS*, 466, 4731, doi: [10.1093/mnras/stw3371](https://doi.org/10.1093/mnras/stw3371)
- Gonzalez, J. J. 1993, University of California, Santa Cruz
- González Delgado, R. M., Pérez, E., Cid Fernandes, R., et al. 2017, *A&A*, 607, A128, doi: [10.1051/0004-6361/201730883](https://doi.org/10.1051/0004-6361/201730883)
- Gorgas, J., Efstathiou, G., & Aragon Salamanca, A. 1990, *MNRAS*, 245, 217, doi: [10.1093/mnras/245.2.217](https://doi.org/10.1093/mnras/245.2.217)
- Graves, G. J., Faber, S. M., Schiavon, R. P., & Yan, R. 2007, *ApJ*, 671, 243, doi: [10.1086/522325](https://doi.org/10.1086/522325)
- Greene, J. E., Janish, R., Ma, C.-P., et al. 2015, *ApJ*, 807, 11, doi: [10.1088/0004-637X/807/1/11](https://doi.org/10.1088/0004-637X/807/1/11)
- Gregg, M. D. 1992, *ApJ*, 384, 43, doi: [10.1086/170846](https://doi.org/10.1086/170846)
- Gunn, J. E., Siegmund, W. A., Mannery, E. J., et al. 2006, *AJ*, 131, 2332, doi: [10.1086/500975](https://doi.org/10.1086/500975)
- Guzman, R., Lucey, J. R., & Bower, R. G. 1993, *MNRAS*, 265, 731, doi: [10.1093/mnras/265.3.731](https://doi.org/10.1093/mnras/265.3.731)
- Henry, R. B. C., & Worthey, G. 1999, *PASP*, 111, 919, doi: [10.1086/316403](https://doi.org/10.1086/316403)
- Huertas-Company, M., Rodriguez-Gomez, V., Nelson, D., et al. 2019, *MNRAS*, 489, 1859, doi: [10.1093/mnras/stz2191](https://doi.org/10.1093/mnras/stz2191)
- Hyde, J. B., & Bernardi, M. 2009, *MNRAS*, 396, 1171, doi: [10.1111/j.1365-2966.2009.14783.x](https://doi.org/10.1111/j.1365-2966.2009.14783.x)
- Illingworth, G. 1981, in *Structure and Evolution of Normal Galaxies*, ed. S. M. Fall & D. Lynden-Bell, 27–41
- Jablonka, P., Gorgas, J., & Goudfrooij, P. 2007, *A&A*, 474, 763, doi: [10.1051/0004-6361:20066691](https://doi.org/10.1051/0004-6361:20066691)
- Johansson, J., Thomas, D., & Maraston, C. 2012, *MNRAS*, 421, 1908, doi: [10.1111/j.1365-2966.2011.20316.x](https://doi.org/10.1111/j.1365-2966.2011.20316.x)
- Jönsson, H., Allende Prieto, C., Holtzman, J. A., et al. 2018, *AJ*, 156, 126, doi: [10.3847/1538-3881/aad4f5](https://doi.org/10.3847/1538-3881/aad4f5)
- Jørgensen, I. 1999, *MNRAS*, 306, 607, doi: [10.1046/j.1365-8711.1999.02555.x](https://doi.org/10.1046/j.1365-8711.1999.02555.x)
- Kauffmann, G., & Charlot, S. 1998, *MNRAS*, 294, 705, doi: [10.1046/j.1365-8711.1998.01322.x](https://doi.org/10.1046/j.1365-8711.1998.01322.x)
- Kauffmann, G., White, S. D. M., & Guiderdoni, B. 1993, *MNRAS*, 264, 201, doi: [10.1093/mnras/264.1.201](https://doi.org/10.1093/mnras/264.1.201)
- Kawata, D. 2001, *ApJ*, 558, 598, doi: [10.1086/322309](https://doi.org/10.1086/322309)
- Kereš, D., Katz, N., Weinberg, D. H., & Davé, R. 2005, *MNRAS*, 363, 2, doi: [10.1111/j.1365-2966.2005.09451.x](https://doi.org/10.1111/j.1365-2966.2005.09451.x)
- Kobayashi, C. 2004, *MNRAS*, 347, 740, doi: [10.1111/j.1365-2966.2004.07258.x](https://doi.org/10.1111/j.1365-2966.2004.07258.x)
- Kobayashi, C., & Nakasato, N. 2011, *ApJ*, 729, 16, doi: [10.1088/0004-637X/729/1/16](https://doi.org/10.1088/0004-637X/729/1/16)
- Koleva, M., Prugniel, P., Bouchard, A., & Wu, Y. 2009a, *A&A*, 501, 1269, doi: [10.1051/0004-6361/200811467](https://doi.org/10.1051/0004-6361/200811467)
- Koleva, M., Prugniel, P., De Rijcke, S., Zeilinger, W. W., & Michielsen, D. 2009b, *Astronomische Nachrichten*, 330, 960, doi: [10.1002/asna.200911272](https://doi.org/10.1002/asna.200911272)
- Kroupa, P. 2001, *MNRAS*, 322, 231, doi: [10.1046/j.1365-8711.2001.04022.x](https://doi.org/10.1046/j.1365-8711.2001.04022.x)
- Kuntschner, H. 2000, *MNRAS*, 315, 184, doi: [10.1046/j.1365-8711.2000.03377.x](https://doi.org/10.1046/j.1365-8711.2000.03377.x)
- Kuntschner, H., Emsellem, E., Bacon, R., et al. 2010, *MNRAS*, 408, 97, doi: [10.1111/j.1365-2966.2010.17161.x](https://doi.org/10.1111/j.1365-2966.2010.17161.x)
- La Barbera, F., Vazdekis, A., Ferreras, I., et al. 2017, *MNRAS*, 464, 3597, doi: [10.1093/mnras/stw2407](https://doi.org/10.1093/mnras/stw2407)
- Lara-López, M. A., Bongiovanni, A., Cepa, J., et al. 2010, *A&A*, 519, A31, doi: [10.1051/0004-6361/200913886](https://doi.org/10.1051/0004-6361/200913886)
- Larson, R. B. 1974, *MNRAS*, 166, 585, doi: [10.1093/mnras/166.3.585](https://doi.org/10.1093/mnras/166.3.585)
- . 1976, *MNRAS*, 176, 31, doi: [10.1093/mnras/176.1.31](https://doi.org/10.1093/mnras/176.1.31)
- Law, D. R., Westfall, K. B., Bershadsky, M. A., et al. 2021, *AJ*, 161, 52, doi: [10.3847/1538-3881/abcaa2](https://doi.org/10.3847/1538-3881/abcaa2)
- Li, Y., Bresolin, F., & Kennicutt, Robert C., J. 2013, *ApJ*, 766, 17, doi: [10.1088/0004-637X/766/1/17](https://doi.org/10.1088/0004-637X/766/1/17)
- Loewenstein, M., & Mathews, W. G. 1987, *ApJ*, 319, 614, doi: [10.1086/165482](https://doi.org/10.1086/165482)
- Magoulas, C., Springob, C. M., Colless, M., et al. 2012, *MNRAS*, 427, 245, doi: [10.1111/j.1365-2966.2012.21421.x](https://doi.org/10.1111/j.1365-2966.2012.21421.x)
- Marigo, P. 2001, *A&A*, 370, 194, doi: [10.1051/0004-6361:20000247](https://doi.org/10.1051/0004-6361:20000247)
- Marigo, P., Girardi, L., Bressan, A., et al. 2008, *A&A*, 482, 883, doi: [10.1051/0004-6361:20078467](https://doi.org/10.1051/0004-6361:20078467)
- Marinacci, F., Vogelsberger, M., Pakmor, R., et al. 2018, *MNRAS*, 480, 5113, doi: [10.1093/mnras/sty2206](https://doi.org/10.1093/mnras/sty2206)
- Martig, M., Fouesneau, M., Rix, H.-W., et al. 2016, *MNRAS*, 456, 3655, doi: [10.1093/mnras/stv2830](https://doi.org/10.1093/mnras/stv2830)
- Martín-Navarro, I., Pérez-González, P. G., Trujillo, I., et al. 2015, *ApJL*, 798, L4, doi: [10.1088/2041-8205/798/1/L4](https://doi.org/10.1088/2041-8205/798/1/L4)
- Martins, L. P., & Coelho, P. 2007, *MNRAS*, 381, 1329, doi: [10.1111/j.1365-2966.2007.11954.x](https://doi.org/10.1111/j.1365-2966.2007.11954.x)
- Matteucci, F. 1996, in *Astronomical Society of the Pacific Conference Series*, Vol. 98, *From Stars to Galaxies: the Impact of Stellar Physics on Galaxy Evolution*, ed. C. Leitherer, U. Fritze-von-Alvensleben, & J. Huchra, 529

- Mehlert, D., Thomas, D., Saglia, R. P., Bender, R., & Wegner, G. 2003, *A&A*, 407, 423, doi: [10.1051/0004-6361:20030886](https://doi.org/10.1051/0004-6361:20030886)
- Melioli, C., Brighenti, F., & D’Ercole, A. 2015, *MNRAS*, 446, 299, doi: [10.1093/mnras/stu2008](https://doi.org/10.1093/mnras/stu2008)
- Montes, M., Trujillo, I., Prieto, M. A., & Acosta-Pulido, J. A. 2014, *MNRAS*, 439, 990, doi: [10.1093/mnras/stu037](https://doi.org/10.1093/mnras/stu037)
- Naiman, J. P., Pillepich, A., Springel, V., et al. 2018, *MNRAS*, 477, 1206, doi: [10.1093/mnras/sty618](https://doi.org/10.1093/mnras/sty618)
- Nelson, D., Pillepich, A., Springel, V., et al. 2018, *MNRAS*, 475, 624, doi: [10.1093/mnras/stx3040](https://doi.org/10.1093/mnras/stx3040)
- Nelson, D., Springel, V., Pillepich, A., et al. 2019, *Computational Astrophysics and Cosmology*, 6, 2, doi: [10.1186/s40668-019-0028-x](https://doi.org/10.1186/s40668-019-0028-x)
- Nomoto, K., Kobayashi, C., & Tominaga, N. 2013, *ARA&A*, 51, 457, doi: [10.1146/annurev-astro-082812-140956](https://doi.org/10.1146/annurev-astro-082812-140956)
- Ogando, R. L. C., Maia, M. A. G., Chiappini, C., et al. 2005, *ApJL*, 632, L61, doi: [10.1086/497824](https://doi.org/10.1086/497824)
- Oppenheimer, B. D., & Davé, R. 2008, *MNRAS*, 387, 577, doi: [10.1111/j.1365-2966.2008.13280.x](https://doi.org/10.1111/j.1365-2966.2008.13280.x)
- Oser, L., Ostriker, J. P., Naab, T., Johansson, P. H., & Burkert, A. 2010, *ApJ*, 725, 2312, doi: [10.1088/0004-637X/725/2/2312](https://doi.org/10.1088/0004-637X/725/2/2312)
- Parikh, T., Thomas, D., Maraston, C., et al. 2021, *MNRAS*, 502, 5508, doi: [10.1093/mnras/stab449](https://doi.org/10.1093/mnras/stab449)
- . 2018, *MNRAS*, 477, 3954, doi: [10.1093/mnras/sty785](https://doi.org/10.1093/mnras/sty785)
- . 2019, *MNRAS*, 483, 3420, doi: [10.1093/mnras/sty3339](https://doi.org/10.1093/mnras/sty3339)
- Partridge, R. B., & Peebles, P. J. E. 1967, *ApJ*, 147, 868, doi: [10.1086/149079](https://doi.org/10.1086/149079)
- Peebles, M. S., & Shankar, F. 2011, *MNRAS*, 417, 2962, doi: [10.1111/j.1365-2966.2011.19456.x](https://doi.org/10.1111/j.1365-2966.2011.19456.x)
- Peletier, R. 1989, *Elliptical galaxies. Structure and stellar content* (University of Groningen, The Netherlands)
- Pillepich, A., Nelson, D., Hernquist, L., et al. 2018, *MNRAS*, 475, 648, doi: [10.1093/mnras/stx3112](https://doi.org/10.1093/mnras/stx3112)
- Pipino, A., D’Ercole, A., Chiappini, C., & Matteucci, F. 2010, *MNRAS*, 407, 1347, doi: [10.1111/j.1365-2966.2010.17007.x](https://doi.org/10.1111/j.1365-2966.2010.17007.x)
- Pipino, A., Matteucci, F., & Chiappini, C. 2006, *ApJ*, 638, 739, doi: [10.1086/499033](https://doi.org/10.1086/499033)
- Poggianti, B. M., Bridges, T. J., Mobasher, B., et al. 2001, *ApJ*, 562, 689, doi: [10.1086/323217](https://doi.org/10.1086/323217)
- Price, J., Phillipps, S., Huxor, A., Smith, R. J., & Lucey, J. R. 2011, *Monthly Notices of the Royal Astronomical Society*, 411, 2558, doi: [10.1111/j.1365-2966.2010.17862.x](https://doi.org/10.1111/j.1365-2966.2010.17862.x)
- Proctor, R. N., Forbes, D. A., Forestell, A., & Gebhardt, K. 2005, *MNRAS*, 362, 857, doi: [10.1111/j.1365-2966.2005.09312.x](https://doi.org/10.1111/j.1365-2966.2005.09312.x)
- Prugniel, P., & Soubiran, C. 2001, *A&A*, 369, 1048, doi: [10.1051/0004-6361:20010163](https://doi.org/10.1051/0004-6361:20010163)
- Pulsoni, C., Gerhard, O., Arnaboldi, M., et al. 2020, *A&A*, 641, A60, doi: [10.1051/0004-6361/202038253](https://doi.org/10.1051/0004-6361/202038253)
- Rawle, T. D., Smith, R. J., & Lucey, J. R. 2010, *MNRAS*, 401, 852, doi: [10.1111/j.1365-2966.2009.15722.x](https://doi.org/10.1111/j.1365-2966.2009.15722.x)
- Rawle, T. D., Smith, R. J., Lucey, J. R., & Swinbank, A. M. 2008, *MNRAS*, 389, 1891, doi: [10.1111/j.1365-2966.2008.13720.x](https://doi.org/10.1111/j.1365-2966.2008.13720.x)
- Rayner, J. T., Toomey, D. W., Onaka, P. M., et al. 2003, *PASP*, 115, 362, doi: [10.1086/367745](https://doi.org/10.1086/367745)
- Romano, D., Karakas, A. I., Tosi, M., & Matteucci, F. 2010, *A&A*, 522, A32, doi: [10.1051/0004-6361/201014483](https://doi.org/10.1051/0004-6361/201014483)
- Roškar, R., Debattista, V. P., Quinn, T. R., Stinson, G. S., & Wadsley, J. 2008a, *ApJL*, 684, L79, doi: [10.1086/592231](https://doi.org/10.1086/592231)
- Roškar, R., Debattista, V. P., Stinson, G. S., et al. 2008b, *ApJL*, 675, L65, doi: [10.1086/586734](https://doi.org/10.1086/586734)
- Sánchez, S. E., Kennicutt, R. C., Gil de Paz, A., et al. 2012, *A&A*, 538, A8, doi: [10.1051/0004-6361/201117353](https://doi.org/10.1051/0004-6361/201117353)
- Sánchez Almeida, J., Morales-Luis, A. B., Muñoz-Tuñón, C., et al. 2014, *ApJ*, 783, 45, doi: [10.1088/0004-637X/783/1/45](https://doi.org/10.1088/0004-637X/783/1/45)
- Sánchez-Blázquez, P., Forbes, D. A., Strader, J., Brodie, J., & Proctor, R. 2007, *MNRAS*, 377, 759, doi: [10.1111/j.1365-2966.2007.11647.x](https://doi.org/10.1111/j.1365-2966.2007.11647.x)
- Sánchez-Blázquez, P., Peletier, R. E., Jiménez-Vicente, J., et al. 2006, *MNRAS*, 371, 703, doi: [10.1111/j.1365-2966.2006.10699.x](https://doi.org/10.1111/j.1365-2966.2006.10699.x)
- Schaye, J., Crain, R. A., Bower, R. G., et al. 2015, *MNRAS*, 446, 521, doi: [10.1093/mnras/stu2058](https://doi.org/10.1093/mnras/stu2058)
- Schiavon, R. P. 2007, *ApJS*, 171, 146, doi: [10.1086/511753](https://doi.org/10.1086/511753)
- Sellwood, J. A., & Binney, J. J. 2002, *MNRAS*, 336, 785, doi: [10.1046/j.1365-8711.2002.05806.x](https://doi.org/10.1046/j.1365-8711.2002.05806.x)
- Sérsic, J. L. 1963, *Boletín de la Asociación Argentina de Astronomía La Plata Argentina*, 6, 41
- Serven, J., Worthey, G., & Briley, M. M. 2005, *ApJ*, 627, 754, doi: [10.1086/430400](https://doi.org/10.1086/430400)
- Serven, J., Worthey, G., Toloba, E., & Sánchez-Blázquez, P. 2011, *AJ*, 141, 184, doi: [10.1088/0004-6256/141/6/184](https://doi.org/10.1088/0004-6256/141/6/184)
- Sil’chenko, O. K. 2015, *Astronomical and Astrophysical Transactions*, 29, 9
- Smee, S. A., Gunn, J. E., Uomoto, A., et al. 2013, *AJ*, 146, 32, doi: [10.1088/0004-6256/146/2/32](https://doi.org/10.1088/0004-6256/146/2/32)
- Somerville, R. S., & Davé, R. 2015, *ARA&A*, 53, 51, doi: [10.1146/annurev-astro-082812-140951](https://doi.org/10.1146/annurev-astro-082812-140951)
- Spitoni, E., Matteucci, F., Recchi, S., Cescutti, G., & Pipino, A. 2009, *A&A*, 504, 87, doi: [10.1051/0004-6361/200911768](https://doi.org/10.1051/0004-6361/200911768)
- Spolaor, M., Proctor, R. N., Forbes, D. A., & Couch, W. J. 2009, *ApJL*, 691, L138, doi: [10.1088/0004-637X/691/2/L138](https://doi.org/10.1088/0004-637X/691/2/L138)
- Springel, V., Di Matteo, T., & Hernquist, L. 2005, *MNRAS*, 361, 776, doi: [10.1111/j.1365-2966.2005.09238.x](https://doi.org/10.1111/j.1365-2966.2005.09238.x)
- Springel, V., Pakmor, R., Pillepich, A., et al. 2018, *MNRAS*, 475, 676, doi: [10.1093/mnras/stx3304](https://doi.org/10.1093/mnras/stx3304)
- Sybiliska, A., Kuntschner, H., van de Ven, G., et al. 2018, *Monthly Notices of the Royal Astronomical Society*, 476, 4501, doi: [10.1093/mnras/sty534](https://doi.org/10.1093/mnras/sty534)
- Tang, B., Worthey, G., & Davis, A. B. 2014, *MNRAS*, 445, 1538, doi: [10.1093/mnras/stu1867](https://doi.org/10.1093/mnras/stu1867)

- Taranu, D., Dubinski, J., & Yee, H. K. C. 2015, in IAU General Assembly, Vol. 29, 2256542
- Thomas, D., Greggio, L., & Bender, R. 1999, MNRAS, 302, 537, doi: [10.1046/j.1365-8711.1999.02138.x](https://doi.org/10.1046/j.1365-8711.1999.02138.x)
- Thomas, D., Maraston, C., & Bender, R. 2003, MNRAS, 339, 897, doi: [10.1046/j.1365-8711.2003.06248.x](https://doi.org/10.1046/j.1365-8711.2003.06248.x)
- Thomas, D., Maraston, C., Bender, R., & Mendes de Oliveira, C. 2005, ApJ, 621, 673, doi: [10.1086/426932](https://doi.org/10.1086/426932)
- Thomas, D., Maraston, C., Schawinski, K., Sarzi, M., & Silk, J. 2010, MNRAS, 404, 1775, doi: [10.1111/j.1365-2966.2010.16427.x](https://doi.org/10.1111/j.1365-2966.2010.16427.x)
- Timmes, F., Woosley, S., & Weaver, T. 1995, Astrophysical Journal, Supplement Series, 98, 617, doi: [10.1086/192172](https://doi.org/10.1086/192172)
- Tinsley, B. M. 1979, ApJ, 229, 1046, doi: [10.1086/157039](https://doi.org/10.1086/157039)
- Tinsley, B. M., & Larson, Richard B. Gehret, D. C., eds. 1977, Evolution of galaxies and stellar populations
- Tiwari, J., Mahajan, S., & Singh, K. P. 2020, NewA, 81, 101417, doi: [10.1016/j.newast.2020.101417](https://doi.org/10.1016/j.newast.2020.101417)
- Toomre, A., & Toomre, J. 1972, ApJ, 178, 623, doi: [10.1086/151823](https://doi.org/10.1086/151823)
- Trager, S. C., Faber, S. M., Worthey, G., & González, J. J. 2000a, AJ, 119, 1645, doi: [10.1086/301299](https://doi.org/10.1086/301299)
- . 2000b, AJ, 120, 165, doi: [10.1086/301442](https://doi.org/10.1086/301442)
- Trager, S. C., Worthey, G., Faber, S. M., Burstein, D., & González, J. J. 1998, ApJS, 116, 1, doi: [10.1086/313099](https://doi.org/10.1086/313099)
- Tremonti, C. A., Heckman, T. M., Kauffmann, G., et al. 2004, ApJ, 613, 898, doi: [10.1086/423264](https://doi.org/10.1086/423264)
- Valdes, F., Gupta, R., Rose, J. A., Singh, H. P., & Bell, D. J. 2004, ApJS, 152, 251, doi: [10.1086/386343](https://doi.org/10.1086/386343)
- van Dokkum, P., Conroy, C., Villaume, A., Brodie, J., & Romanowsky, A. J. 2017, ApJ, 841, 68, doi: [10.3847/1538-4357/aa7135](https://doi.org/10.3847/1538-4357/aa7135)
- Vazdekis, A., Sánchez-Blázquez, P., Falcón-Barroso, J., et al. 2010, MNRAS, 404, 1639, doi: [10.1111/j.1365-2966.2010.16407.x](https://doi.org/10.1111/j.1365-2966.2010.16407.x)
- Vogelsberger, M., Genel, S., Springel, V., et al. 2014a, MNRAS, 444, 1518, doi: [10.1093/mnras/stu1536](https://doi.org/10.1093/mnras/stu1536)
- . 2014b, Nature, 509, 177, doi: [10.1038/nature13316](https://doi.org/10.1038/nature13316)
- Walcher, J., Groves, B., Budavári, T., & Dale, D. 2011, Ap&SS, 331, 1, doi: [10.1007/s10509-010-0458-z](https://doi.org/10.1007/s10509-010-0458-z)
- Weinberg, D. H., Andrews, B. H., & Freudenburg, J. 2017, ApJ, 837, 183, doi: [10.3847/1538-4357/837/2/183](https://doi.org/10.3847/1538-4357/837/2/183)
- Westfall, K. B., Cappellari, M., Bershad, M. A., et al. 2019, AJ, 158, 231, doi: [10.3847/1538-3881/ab44a2](https://doi.org/10.3847/1538-3881/ab44a2)
- White, S. D. M. 1980, MNRAS, 191, 1P, doi: [10.1093/mnras/191.1.1P](https://doi.org/10.1093/mnras/191.1.1P)
- Woosley, S. E., & Weaver, T. A. 1995, ApJS, 101, 181, doi: [10.1086/192237](https://doi.org/10.1086/192237)
- Worthey, G. 1994, ApJS, 95, 107, doi: [10.1086/192096](https://doi.org/10.1086/192096)
- . 1998, PASP, 110, 888, doi: [10.1086/316203](https://doi.org/10.1086/316203)
- Worthey, G., España, A., MacArthur, L. A., & Courteau, S. 2005, ApJ, 631, 820, doi: [10.1086/432785](https://doi.org/10.1086/432785)
- Worthey, G., Faber, S. M., & Gonzalez, J. J. 1992, ApJ, 398, 69, doi: [10.1086/171836](https://doi.org/10.1086/171836)
- Worthey, G., Faber, S. M., Gonzalez, J. J., & Burstein, D. 1994, ApJS, 94, 687, doi: [10.1086/192087](https://doi.org/10.1086/192087)
- Worthey, G., Ingermann, B. A., & Serven, J. 2011, ApJ, 729, 148, doi: [10.1088/0004-637X/729/2/148](https://doi.org/10.1088/0004-637X/729/2/148)
- Worthey, G., Shi, X., Pal, T., Lee, H.-c., & Tang, B. 2022, MNRAS, 511, 3198, doi: [10.1093/mnras/stac267](https://doi.org/10.1093/mnras/stac267)
- Worthey, G., Tang, B., & Serven, J. 2014, ApJ, 783, 20, doi: [10.1088/0004-637X/783/1/20](https://doi.org/10.1088/0004-637X/783/1/20)
- Worthey, G., Trager, S. C., & Faber, S. M. 1995, in Astronomical Society of the Pacific Conference Series, Vol. 86, Fresh Views of Elliptical Galaxies, ed. A. Buzzoni, A. Renzini, & A. Serrano, 203
- Yan, R., Chen, Y., Lazarz, D., et al. 2019, ApJ, 883, 175, doi: [10.3847/1538-4357/ab3ebc](https://doi.org/10.3847/1538-4357/ab3ebc)
- Zaritsky, D., Kennicutt, Robert C., J., & Huchra, J. P. 1994, ApJ, 420, 87, doi: [10.1086/173544](https://doi.org/10.1086/173544)